





RESEARCH ARTICLE | AUGUST 31 2023

## Acceleration and Reynolds effects of crosswind flow fields in gorge terrains

Jian Wang (王剑) ; Xin-Yuan Liu (刘新源); E Deng (邓鐸)  ; Yi-Qing Ni (倪一清) ;  
Pak-Wai Chan (陈柏纬); Wei-Chao Yang (杨伟超); Yan-Ke Tan (谭俨珂)



*Physics of Fluids* 35, 085143 (2023)

<https://doi.org/10.1063/5.0165513>



View  
Online



Export  
Citation

### Articles You May Be Interested In

Crosswind-induced aero-performance deterioration of a vehicle passing by a hill with different windproof measures

*Physics of Fluids* (January 2025)

Wake dynamic characteristics of windproof structures in embankment–bridge sections along a high-speed railway under natural strong crosswinds

*Physics of Fluids* (May 2023)

Flow characteristics induced by a multiform windbreak in complex terrains with and without a train: A simplified method for calculating aerodynamic loads

*Physics of Fluids* (December 2024)



Physics of Fluids

Special Topics Open  
for Submissions

[Learn More](#)

# Acceleration and Reynolds effects of crosswind flow fields in gorge terrains

Cite as: Phys. Fluids **35**, 085143 (2023); doi: [10.1063/5.0165513](https://doi.org/10.1063/5.0165513)

Submitted: 29 June 2023 · Accepted: 22 August 2023 ·

Published Online: 31 August 2023



View Online



Export Citation



CrossMark

Jian Wang (王剑),<sup>1</sup> Xin-Yuan Liu (刘新源),<sup>2,3</sup> E Deng (邓铿),<sup>2,3,a)</sup> Yi-Qing Ni (倪一清),<sup>2,3</sup> Pak-Wai Chan (陈柏纬),<sup>4</sup> Wei-Chao Yang (杨伟超),<sup>1,5</sup> and Yan-Ke Tan (谭侃珂)<sup>2,3,6</sup>

## AFFILIATIONS

<sup>1</sup>School of Civil Engineering, Central South University, Changsha, Hunan 410075, China

<sup>2</sup>National Rail Transit Electrification and Automation Engineering Technology Research Center (Hong Kong Branch), Hong Kong, China

<sup>3</sup>Department of Civil and Environmental Engineering, The Hong Kong Polytechnic University, Hong Kong, China

<sup>4</sup>Hong Kong Observatory, Hong Kong, China

<sup>5</sup>National Engineering Research Center of High-speed Railway Construction Technology, Central South University, Changsha, Hunan 410075, China

<sup>6</sup>College of Civil Engineering, Tongji University, Yangpu District, Shanghai, China

<sup>a)</sup> Author to whom correspondence should be addressed: [early.deng@polyu.edu.hk](mailto:early.deng@polyu.edu.hk)

## ABSTRACT

A significant acceleration generated in the gorge terrain poses a serious threat to the operational safety of the transportation facilities downstream of the gorge. To determine the formation mechanism of the acceleration effect, this paper compares the results of wind tunnel tests with the improved delayed detached eddy simulation in terms of the spatial distribution, turbulence, and spectrum of the flow field on the gorge topography under crosswinds. The effect of the Reynolds number on the results is discussed in terms of the characteristic wind speed of flow field and the scaling ratio. Recurrent neural networks are used to attempt to get signals from unknown measurement points and to repair damaged signals. The results show that when the mountain spacing in the experimental and the computational fluid dynamics models is zero, the most dramatic acceleration reaches 1.28–1.4 times the incoming wind speed. In the wind tunnel tests, the peak of the power spectra density ( $1.065 \times 10^{-2}$ ) at the downstream of the center of the gorge with a mountain spacing of zero is 3.37 and 14.77 times higher than the corresponding values ( $3.16 \times 10^{-3}$  and  $7.21 \times 10^{-4}$ ) in the gorge topography with the mountain spacing of 0.01 and 0.02 m, respectively. The maximum difference of mean wind velocities in the leeward of the gorge is 6.4% when the Reynolds number ranges from  $2.03 \times 10^5$  to  $1.03 \times 10^7$ . The results are expected to provide a reference for the design of windproof facilities in gorge terrains.

Published under an exclusive license by AIP Publishing. <https://doi.org/10.1063/5.0165513>

## I. INTRODUCTION

Areas such as mountainous hills and ravines have more complex topographical features than plains and plateaus. Factors including the difference in the temperature, the gap in pressure, and the bypass effect of the hilly topography disrupt the stable structure of the flow field under a relatively steady incoming wind. In particular, when the incoming flow passes through a gorge formed by two mountains (Fig. 1), a significant increase in wind speed and a variable in wind direction are caused by the slope of the mountain and the narrow passages. The effect of acceleration usually leads to a significant temporal and spatial inconstancy in the wind field.<sup>1,2</sup> In addition, the vortices shed on the surface of the mountain under the action of crosswinds will cause vortex-excited vibrations in the structures downstream, and

this poses a threat to the stability of the structure.<sup>3</sup> For example, the high-speed trains and the road vehicles frequently traverse the variety of complex topographies during their operation. A complex topography is often closely linked to the generation and development of extreme wind events on the transport route. Many studies have shown that strong crosswinds pose a serious threat to the operational stability and safety of high-speed trains as they can easily cause derailments and even overturning accidents.<sup>4,5</sup> Ensuring the operational safety of high-speed trains when they cross the wind field in this case, compared with stable conditions of crosswind flow, is a daunting challenge.

A large number of studies have been devoted to field tests,<sup>6,7</sup> wind tunnel tests,<sup>8–11</sup> and computational fluid dynamics (CFD) simulations<sup>12–14</sup> to characterize and predict the wind field under complex



FIG. 1. The topography of a gorge formed by two mountains.

topographical conditions. Jing *et al.*<sup>15</sup> analyzed the characteristics of the wind field of a gorge by using two wind masts and showed that the average direction of wind at high speeds was always along the wall of the gorge. The research is valuable for engineering measurement strategies in gorge terrain. However, it is difficult to obtain the structure of the wind field of an entire gorge due to the sparsity of the points of measurement. Song *et al.*<sup>16</sup> studied the characteristics of the wind field in a valley by means of a Doppler sodar system mounted on a bridge and supplemented their study with a wind tunnel test at the scale of 1:1500. In addition, the team used the Standard  $k$ - $\epsilon$  model to numerically simulate the flow field of a bridge on the Yellow River on a topography with a converging channel.<sup>17</sup> They found that the airflow accelerated at the outlet of the valley, with a significant non-uniformity in the speed and direction of wind on the bridge along the longitudinal direction. However, they did not discuss the generation mechanism of the acceleration effect and the influence of the scaling ratio on the results. Ren *et al.*<sup>18</sup> arranged five anemometers along the longitudinal direction on a mountainous bridge for long-term observations and analyzed the characteristics of the wind field by using a traditional model of stable wind speed and a model of non-constant wind speed. This study focuses on the effects of two wind speed models on the wind field, which gives a model reference for wind field studies in gorge terrain. However, this study does not show the complete characterization of the entire wind field. Zhou *et al.*<sup>19</sup> and Deng *et al.*<sup>20</sup> used CFD simulations to study the effects of mountain topographies on the wind field. Some researchers have also conducted multi-scale numerical simulations of turbulence in the wind field in a realistic and complex topography based on weather research and forecasting-large eddy

simulation (WRF-LES).<sup>21</sup> These reveal that the wind field in a gorge undergoes a significant acceleration and has non-stationary characteristics. McGrath *et al.*<sup>22</sup> established a high-fidelity, physics-based modeling and simulation framework in order to study the aerodynamic behavior of unmanned aerial systems (UAS) in complex terrain. The framework facilitates the study of the flight attitude of a craft in complex terrain. However, the above-mentioned studies have not systematically parametrized the geometric features of the topography and have ignored the influence of the spacing between mountains forming a gorge on the acceleration in the speed of wind flowing through it.

To alleviate the threat posed by a strong crosswind on the operational stability and security of high-speed trains, many researchers have proposed a number of mitigation measures, including wind barriers,<sup>23–25</sup> windbreaks,<sup>26,27</sup> and anti-wind open-cut tunnels,<sup>28</sup> in which such parameters as the curvature of the profile and porosity of the wind barriers have a large impact on the aerodynamic performance of bridges and high-speed trains.<sup>29</sup> Chen *et al.*<sup>30</sup> found that abrupt changes in the structure of the wind barrier in the longitudinal direction under strong crosswinds lead to a deterioration in the aerodynamic performance of high-speed trains. There are abrupt changes in the structure of most wind barriers due to limitations of the terrain in reality, which results in anti-wind measures not being as effective as expected. Yang *et al.*<sup>31</sup> analyzed transient aerodynamic loads on high-speed trains based on CFD simulations and compared the anti-wind performance of a windbreak and an anti-wind open-cut tunnel. The results showed that the aerodynamic load on the vehicle exhibited large fluctuations under the same conditions of crosswinds for the windbreak, and suddenly and significantly increased or decreased at

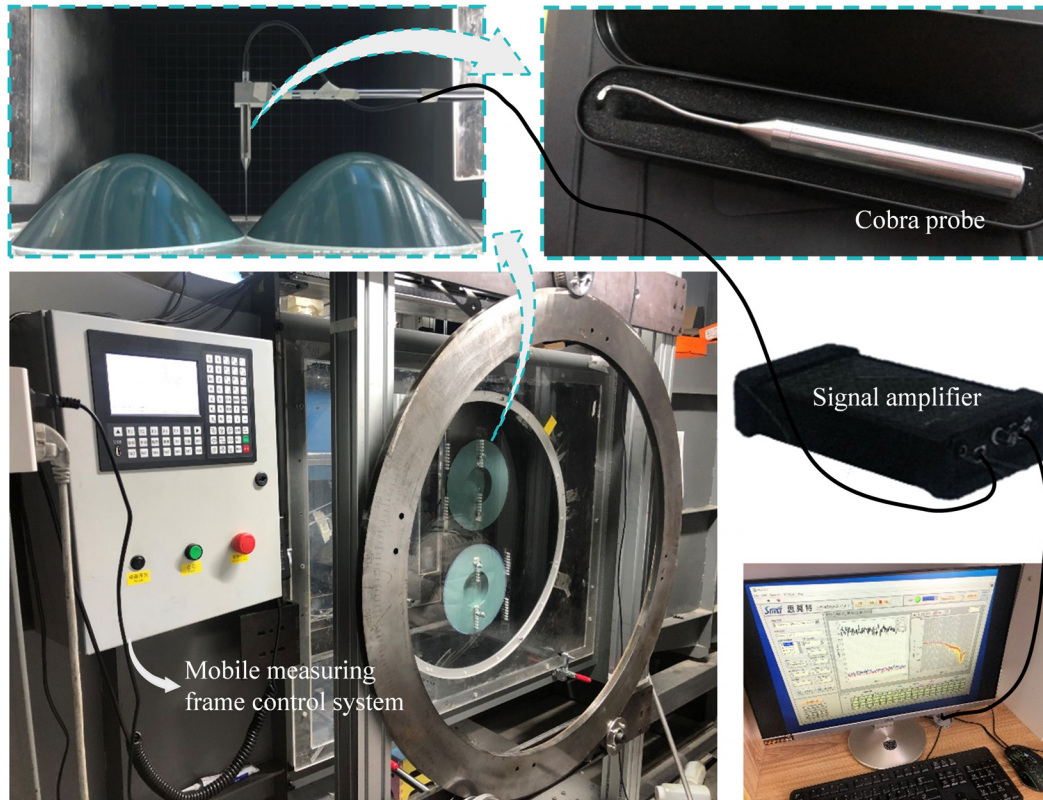


FIG. 2. The wind tunnel test system for the topography of the gorge.

the end of the windproof facilities. It is clear from the above that most studies in the area have used traditional, passive, anti-wind facilities, such as wind barriers, the capability of wind resistance of which is limited. Therefore, it is necessary to propose an effective active anti-wind measure in harsh wind environments.

To determine the influence of the spacing between mountains on such an acceleration, this study compares the results of wind tunnel tests with the improved delayed detached eddy simulation in terms of the characterization of the flow field on the gorge topography under crosswinds. The effect of the Reynolds number on the results is discussed in terms of the characteristic wind speed of flow field and the scaling ratio. In addition, recurrent neural network (RNN) is used to attempt to get signals from unknown measurement points and to repair damaged signals in wind tunnel tests. Finally, this study proposes an active anti-wind idea based on jet devices. The results of this study provide sound theoretical guidance for the siting and anti-wind design of transportation facilities crossing gorges.

## II. METHODOLOGY

### A. The wind tunnel overview

As shown in Fig. 2, the wind tunnel test system consists of a return-flow wind tunnel, an SMT series 3D dynamic anemometer system, an automatic moving measurement frame, and an experimental model. The shape parameters of the wind tunnel test section and the experimental model are presented in Fig. 3. The length, width, and

height of the wind tunnel test section are 1.8, 1.2, and 0.8 m, respectively, and the frequency of the input AC power to the turbines is continuously adjustable in the range of 0–62 Hz. The test data were collected by using an SMT series 3D dynamic anemometer system with a sampling time of 10 s and a sampling frequency of 1000 Hz at each measurement point. The measurement system consists of a cobra

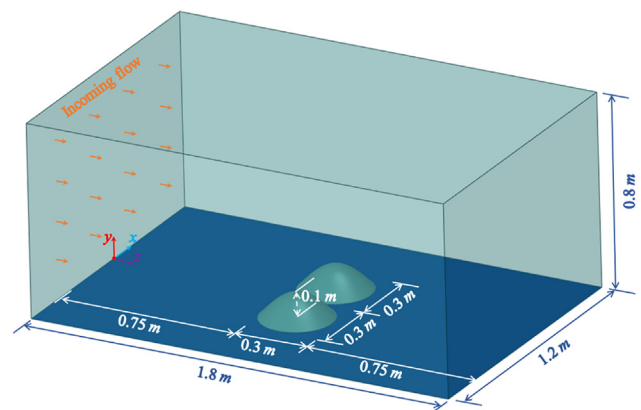
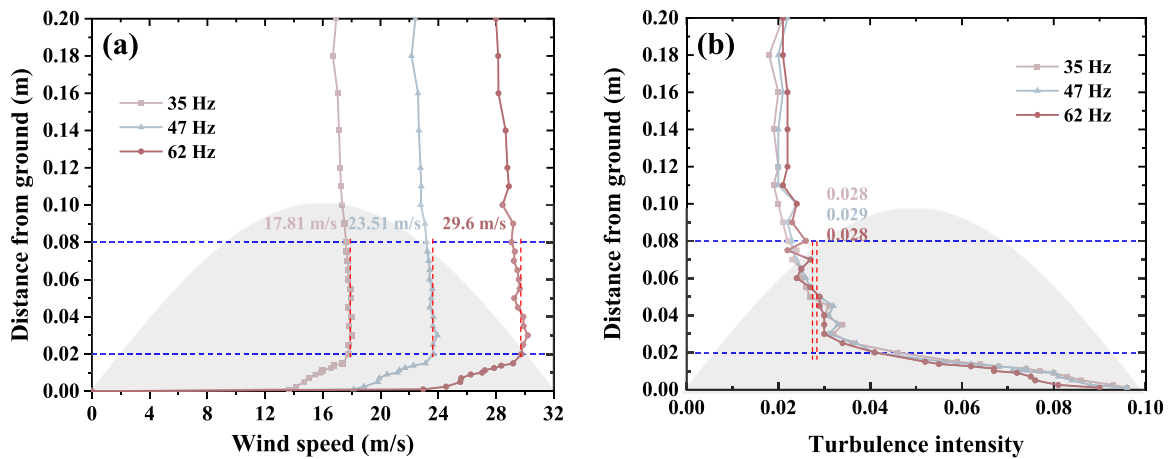


FIG. 3. The shape parameters of the wind tunnel test section and the experimental model.



**FIG. 4.** The distribution of the Z component of the mean wind speed and the mean turbulence intensity along Y direction at the center of the wind tunnel: (a) Wind speed and (b) Turbulence intensity.

probe, a signal amplifier, and a data acquisition terminal. The cobra probe has an accuracy of  $\pm 0.5$  m/s in measured wind speed and  $\pm 1^\circ$  in angle measurement. Due to the fact that obtaining the full wind field characteristics requires combining data from a large number of measurement points, the automatic moving measurement frame is used to reduce the position deviation generated during the movement of the probe. The displacement accuracy of the automatic mobile measuring frame is 0.001 m when moving the measurement point.

Figure 4 presents the Z component of the mean wind speed and the mean turbulence intensity along Y direction at the center of the wind tunnel. Wind speed and turbulence intensity of within 0–0.02 m from the ground varied after the input of 35, 47, and 62 Hz AC in the wind tunnel without the gorge model, which was caused by the effect of the boundary layer. With increasing distance from the ground, the viscous force of the fluid gradually decreased. The Z component of the mean wind speed ( $U$ ) was steady at 17.81, 23.51, and 29.6 m/s, respectively, in the range of distance of 0.02–0.08 m from the ground. The intensity of turbulence was steady at 0.028, 0.029, and 0.028, respectively, in the range of distance of 0.02–0.08 m from the ground.

As shown in Fig. 3, the experimental model is a gorge model consisting of two mountains. The cosine curve defined by Eq. (1) is used in the construction of the mountain, and Liu *et al.*<sup>32</sup> and Yang *et al.*<sup>33</sup> have verified that a cosine shape of their outline is representative. To reduce the influence of blockage rate and boundary layer, the mountain model is built based on a scaling ratio of 1:500. The height ( $H$ ) and bottom diameter ( $D$ ) of the mountain are 0.1 and 0.3 m, respectively. The rate of blockage of the test section of the wind tunnel is 3.99%. Finally, the effect law of the mountain spacing on the acceleration effect is investigated by adjusting the spacing between two mountains. The mountain spacing ( $W$ ) is divided into 0, 0.01, and 0.02 m, and the names of the corresponding experimental models are defined as Case I, Case II, and Case III, respectively. Table I exhibits the parameters of the main research cases in this paper:

$$\begin{cases} y(x, z) = H \cos^2 \pi (x^2 + z^2)^{1/2} / D, & (x^2 + z^2)^{1/2} < D/2, \\ y(x, z) = 0, & (x^2 + z^2)^{1/2} \geq D/2, \end{cases} \quad (1)$$

where  $x$ ,  $y$ , and  $z$  denote the direction of the spread of flow, the vertical direction, and the downstream direction of the computational domain, respectively.  $H$  is the height of the mountain, and  $D$  is the diameter of the circle formed by the bottom of the mountain.

## B. The CFD prediction method

### 1. Geometric features and boundary conditions of CFD models

In this study, CFD numerical models were built based on two kinds of scaling ratios (1:500 and 1:10), in which the geometric characteristics of the CFD numerical models with the scaling ratio of 1:500 were established based on the wind tunnel tests (Fig. 3). The mesh and computational strategy were consistent with the CFD numerical model with the scaling ratio of 1:10. The CFD numerical models of four values of spacings between mountains ( $W'$ ) were established based on a scale of 1:10. The spacings were classified as 0, 0.5, 1, and 7 m, and the corresponding cases were called GM-0, GM-0.5, GM-1, and GM-7, respectively, where the net spacing of GM-7 at a height of 1 m was equal to that of GM-0 at a height of 4 m. The basis for this scheme is introduced in Sec. III C. In addition, a model of the gorge with an air curtain (GMAC) was built based on case GM-0 by using the cosine

**TABLE I.** Parameters of the main research cases.

Cases	Wind tunnel test	IDDES	Scale ratio	Spacing of mountains (m)
Case I	✓	✓	1:500	0
Case II	✓	✓	1:500	0.01
Case III	✓	✓	1:500	0.02
GM-0	...	✓	1:10	0
GM-0.5	...	✓	1:10	0.5
GM-1	...	✓	1:10	1
GM-7	...	✓	1:10	7

curve defined by Eq. (1). To show the installation positions of the jet devices, the geometric features and boundary settings of the model are shown with the GMAC case as an example.

Figure 5 presents the geometric features and the settings of various boundary conditions of the CFD model. The geometric parameters are expressed in terms of the height of the mountain ( $H' = 5$  m) and the diameter of its bottom ( $D' = 15$  m). The entire computational domain was  $5D'$  long in the direction of spreading of flow (X),  $2.33D'$  wide along the downstream direction (Z), and  $2H'$  high along the vertical direction (Y). The two mountain bodies were symmetrically distributed along the direction of spreading of flow of the computational domain, and the minimum distance between the foot of the mountain and the boundary of incoming flow was  $0.333D'$ .

Figure 5 illustrates the boundary conditions of the model of the gorge, where the boundary of incoming flow and the surface of the jet of the air curtain were defined as the inlet of velocity. The top surface of the calculation domain was set to be symmetric. No-slip walls were used for the ground, the surface of the mountain, and the side of the air curtain, and the outlet of pressure was used for the left and right sides of the calculation domain as well as the downstream exit surface. The direction of wind was set along the positive Z axis at the boundary of incoming flow.

## 2. Mesh system and solution strategy

The grid models for this study were constructed by using a poly-hexcore grid. As is shown in Fig. 6, the model of the gorge used the laminated poly mesh near the boundary layer, the region of transition region was discretized by it, and the interior was filled by a hexahedral mesh. To better capture the variation in turbulence near the mountain, the computational domain was divided into two fine regions, R1 and R2. Their locations and dimensions are shown in Fig. 6, where the size

of the mesh of R1 was restricted to 0.05 m and that of R2 to 0.1 m. The range of sizes of the meshes for the face of the mountain and air curtain was limited to 0.002–0.005 m. The surfaces of the mountain and the air curtain were set up with a boundary layer consisting of ten layers (estimated,  $y^+ < 10$ ). The figure also shows the parameters related to the boundary layer settings. Finally, the aggregate number of grid cells for the GMAC case was  $54 \times 10^6$ .

Compared with the Reynolds-averaged Navier–Stokes simulation (RANS) and large eddy simulation (LES), the detached eddy simulation (DES) method has the advantages of high computational accuracy and low computational cost. Therefore, the DES method is often used to numerically predict the three-dimensional characteristics of unsteady turbulence over hilly terrains. However, Risan *et al.*<sup>34</sup> compared the measurements of the long-range pulsed lidar with predictions of the DES model and found that the latter overestimated the mean turbulence on the leeward side of a hilly topography. This phenomenon might have been caused by an improper definition of the length of the grid of the boundary layer during model building, which in turn led to a nonphysical separation and a logarithmic mismatch between the layers. Researchers have continued to improve and optimize the DES model over the years. The delayed detached eddy simulation (DDES) method can avoid the separation phenomenon by controlling the parameters of the boundary layer.<sup>35</sup> In addition, the improved DDES (IDDES) method has been developed to handle the problem of a logarithmic mismatch between layers based on the DDES. Therefore, the IDDES method was used in this paper to predict the structure of turbulence in all models of the gorge. The turbulent kinetic energy according to the IDDES is as follows:

$$\frac{\partial(\rho k)}{\partial t} + \frac{\partial(\rho k \bar{u}_i)}{\partial x_i} = \frac{\partial}{\partial x_j} \left[ \left( \mu + \frac{1}{\sigma_k} \mu_t \right) \frac{\partial k}{\partial x_j} \right] + 2\mu_t S_{ij}^2 - \frac{\rho k^{3/2}}{l}, \quad (2)$$

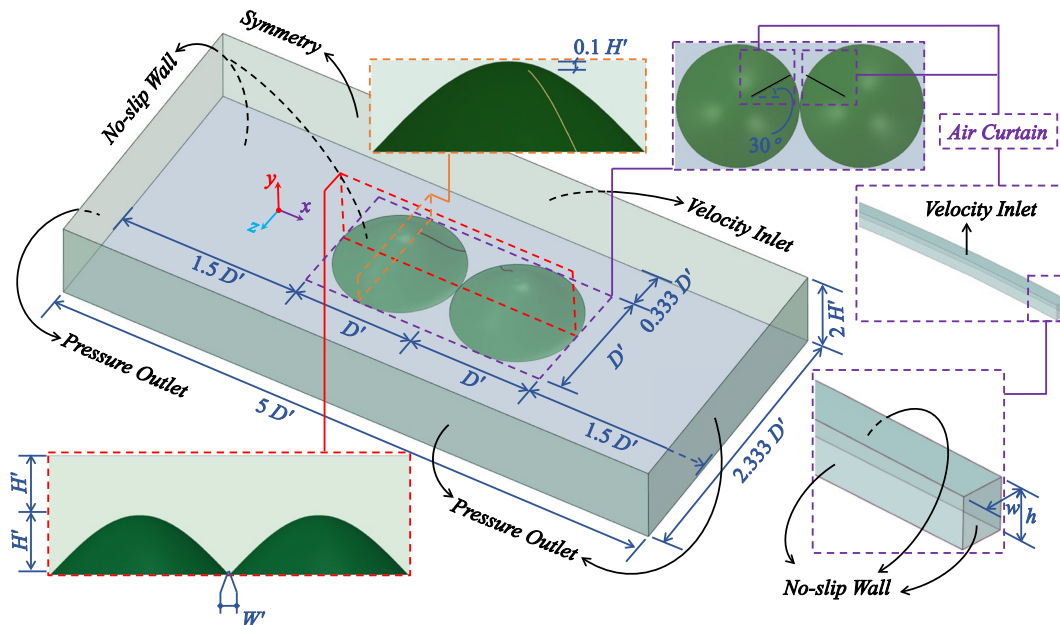


FIG. 5. Geometric features and boundary conditions of the model of the gorge with an air curtain ( $W' = 0$ ).

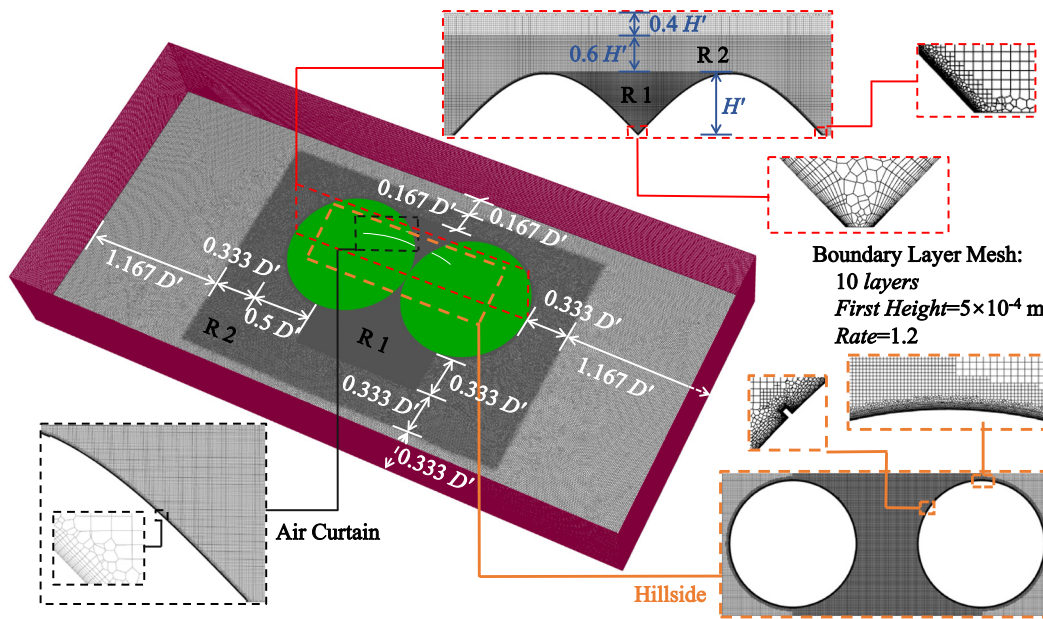


FIG. 6. Mesh model of the model of the gorge with an air curtain ( $W = 0$ ).

$$\frac{\partial(\rho \varepsilon)}{\partial t} + \frac{\partial(\rho \varepsilon \bar{u}_i)}{\partial x_j} = \frac{\partial}{\partial x_j} \left[ \left( \mu + \frac{1}{\sigma_\varepsilon} \mu_t \right) \frac{\partial \varepsilon}{\partial x_j} \right] + 2.88 \mu_t S_{ij}^2 \frac{\varepsilon}{k} - 1.92 \rho \frac{\varepsilon^2}{k}, \quad (3)$$

where  $\rho$ ,  $k$ ,  $\varepsilon$ ,  $\bar{u}_i$ ,  $\mu$ , and  $\mu_t$  are the atmospheric density, turbulent kinetic energy (TKE), rate of dissipation of the TKE, velocity of air-flow, viscosity, and turbulent viscosity, respectively. The values of constants  $\sigma_k$  and  $\sigma_\varepsilon$  are 1 and 1.3, respectively;  $S_{ij}^2$  is the strain rate tensor; and  $l$  is the scale of length of the IDDES, which is calculated as shown in the following equations:

$$l = f_d(1 + f_e)l_{\text{RANS}} + (1 - f_d)C_{\text{DES}}\Delta, \quad (4)$$

$$f_d = \max \left\{ \tanh \left[ \left( A_1 \frac{\nu_t + \nu}{\kappa^2 d^2 U_{ij}} \right)^{A_2} \right], f_{\text{step}} \right\}, \quad (5)$$

$$U_{ij} = \frac{\partial \bar{u}_i}{\partial x_j}, \quad (6)$$

$$\Delta = \min(\max(C_w d, C_w \Delta_{\text{max}}, d_{wn}), \Delta_{\text{max}}), \quad (7)$$

where  $f_d$ ,  $f_e$ ,  $l_{\text{RANS}}$ , and  $\Delta$  are the mixing function, the lifting function, the scale of length of the RANS, and the scale of grid of the IDDES, respectively. In the actual simulations, the constant  $C_{\text{DES}}$  is calibrated by using typical arithmetic examples of isotropic turbulence. The values of the parameters  $A_1$  and  $A_2$  are 20 and 3, respectively.  $\nu_t$ ,  $\nu$ ,  $\kappa$ ,  $d$ , and  $U_{ij}$  are the viscosity of the moving vortex, the molecular viscosity, the von Kármán constant, the distance between the grid cell and the wall, and the velocity gradient, respectively. The function  $f_{\text{step}}$  is used in the IDDES model to quickly switch between the RANS and the LES models near boundary layer. The empirical constant  $C_w$  is set to 0.15;  $\Delta_{\text{max}}$  is the maximal value of the interval of the local mesh; and  $d_{wn}$  is the grid size of the wall along the normal direction.

The transient calculation scheme was used to solve the non-stationary flow field in the topography of the gorge. The time step of calculations for each case was set to 0.001 s, where the number of iterations per time step was 20 and the total number of iterations was  $1 \times 10^4$ . According to the CFL guidelines, it is required that the CFL value should be less than 1 in order to maintain the stability and accuracy of the calculation results. Since the main object of study is the flow field in the R1 or R2 region, the authors obtained a CFL number of 0.6 using a time step  $\Delta t$  ( $\Delta t = 0.001$  s), a grid scale in the R1 region  $\Delta x$  ( $\Delta x = 0.05$  m), and a characteristic flow velocity  $u$  ( $u = 30$  m/s). This indicates that the selected time step is appropriate and does not introduce significant errors. All models of calculation were executed at the Wuxi Supercomputing Center in China by using 120 cores for each, which took a total of 21 days.

### 3. Monitoring strategy

Figure 7 presents the layout of the measurement points and lines in the model of the gorge. One group of measurement lines ( $L_{x1}$ ) was arranged on the leeward side of the mountain along the X direction, and the lines ( $L_{x1-1}$ ,  $L_{x1-2}$ ,  $L_{x1-3}$ , and  $L_{x1-4}$ ) were set at four heights ( $0.2H'$ ,  $0.4H'$ ,  $0.6H'$ , and  $0.8H'$ ). Three measurement lines ( $L_{y1-1}$ ,  $L_{y1-2}$ , and  $L_{y1-3}$ ) were arranged on the leeward side of the gorge along the Y direction, and their range of heights was  $0-1H'$ . Three groups of lines ( $L_{z1}$ ,  $L_{z2}$ , and  $L_{z3}$ ) were arranged on both sides and in the middle of the gorge along the Z direction, and each group of lines was set at four heights ( $0.2H'$ ,  $0.4H'$ ,  $0.6H'$ , and  $0.8H'$ ). In addition, the measurement points (P1, P2, P3, P4, and P5) were arranged on the line  $L_{x1-1}$ . P3 was defined as the typical measurement point in the downstream area of the center of gorge. P2 and P4 were defined as typical measurement points of the central area on the leeward side of the mountain, respectively. P1 and P5 were defined as typical measurement points in

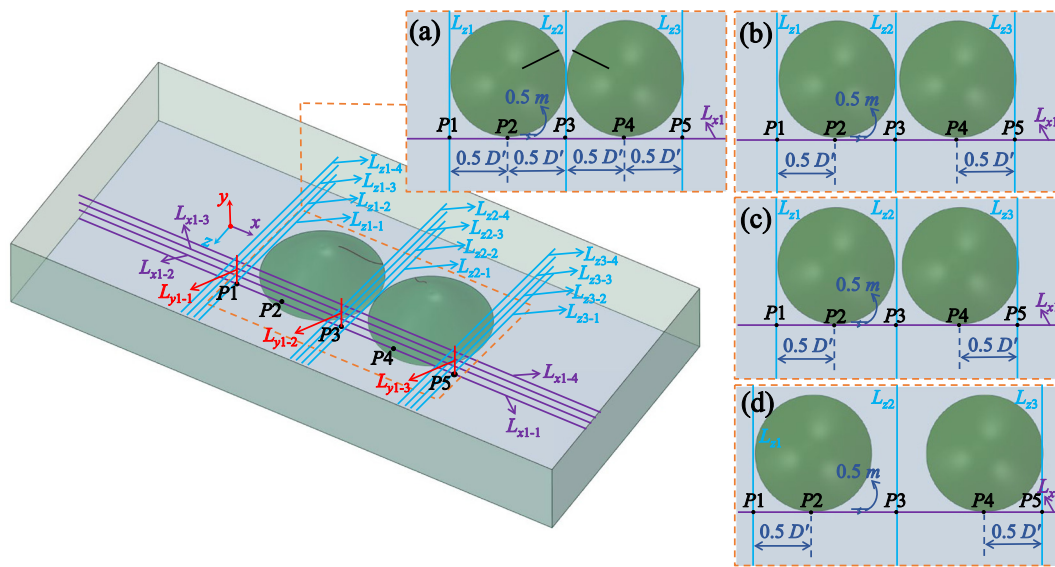


FIG. 7. Layout of typical measurement points and lines: (a) GM-0 and GMAC; (b) GM-0.5; (c) GM-1; and (d) GM-7.

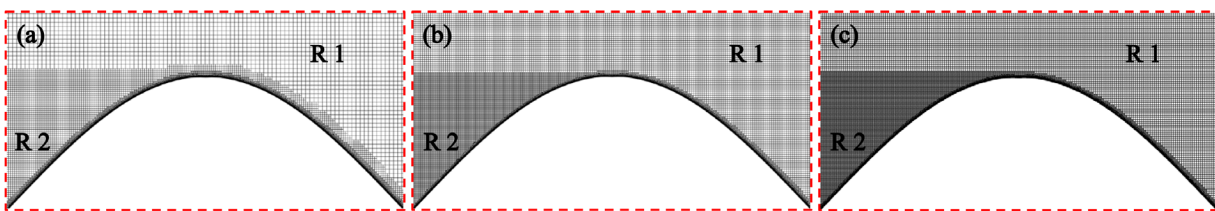


FIG. 8. Profiles of the mountain obtained by using three models with grids of different resolutions: (a) Coarse; (b) Medium; and (c) Fine.

the marginal area of the downstream of the gorge. The 0.5 m implies the minimum distance of the measuring lines  $L_x$  from the foot of the hill in the downstream direction.

#### 4. Independence of grid resolution

To analyze the effect of the resolution of the mesh on the outcomes of calculations of the model, this paper used three grid models for the GM-0 case at three resolutions (coarse, medium, and fine) by resizing the grids in regions R1 and R2 (Fig. 8). The  $U'$  symbol indicates the wind speed of the incoming flow for the gorge model with a scale-down ratio of 1:10. The aggregate numbers of grids for the three calculation models were  $44 \times 10^6$ ,  $54 \times 10^6$ , and  $64 \times 10^6$ , respectively, and the calculation schemes were set according to the procedure detailed in Secs. II B 1 and II B 2. Figure 9 compares the distributions of the component of the mean wind speed in the Z direction on the measurement line  $L_{x1-1}$  from 4 to 10 s for each of the three models of the grid. As is shown in Fig. 9, the results of calculations using the medium and fine grids were in better agreement with each other than with those of the coarse grid (deviation, 5.1%). The model of the grid

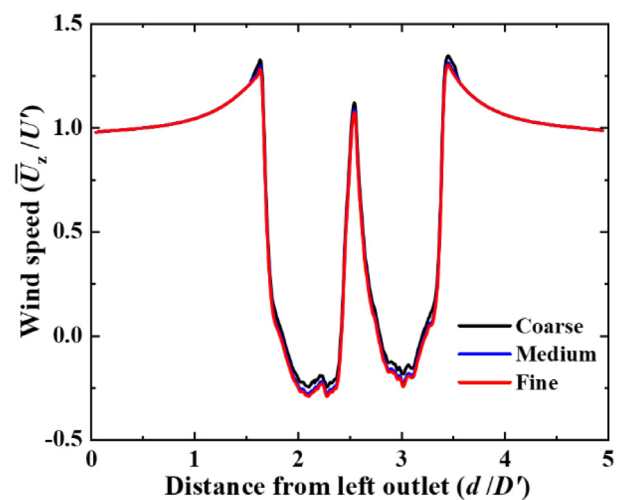


FIG. 9. Distributions of the Z component of the mean wind speed, obtained by the three models with grids of different resolutions on  $L_{x1-1}$ .

with a medium resolution ( $54 \times 10^6$ ) was determined to be suitable for use here.

### III. ANALYSIS OF THE RESULTS

#### A. The wind tunnel test and the CFD prediction method

##### 1. Wind velocity

Figure 10 presents the distribution curves of the Z component of the mean wind speed along the Y-direction measurement line ( $L_1$  and  $L_2$ ) during 4–10 s for the three cases (Case I, Case II, and Case III) based on the wind tunnel tests and the CFD prediction methods, in which the wind speed at the measurement point is dimensionless by the incoming wind speed ( $U = 29.6$  m/s), and the height of the measurement point from the ground is dimensionless by the height of the mountain ( $H = 0.1$  m). In addition, Fig. 10 shows the positions of the different measurement lines in the gorge for the three cases and the corresponding fitting equations. As shown in Fig. 10, there is a significant acceleration effect on the downstream of the outer edge of the gorge and the center of the gorge. As shown in Fig. 10(a), the mean wind speeds at the downstream of the outer edge of the gorge are accelerated to 1.22 and 1.23 times the incoming wind speed ( $U$ ) in the wind tunnel test and the CFD prediction, respectively. From Fig. 10(b), it can be seen that the acceleration effect of the incoming flow becomes more significant as the height of the measurement point at the downstream of the gorge center from the ground increases. Among them, the highest wind speed of  $1.28U$  is measured in the Case I based on the wind tunnel tests, the highest wind speed of  $1.33U$  is measured in the Case I based on the CFD prediction, and the difference between them is maintained at 3.91%. As the distance between the mountains increases, the wind speed at the measurement points in the height range of  $0.2$ – $0.6H$  from the ground gradually increases, which is due to the weakening of the shading effect of the mountains. More incoming flow passes through the gap between the two mountains.

In Fig. 10, the Z-direction mean wind speeds based on the IDDES method on the  $L_1$  measurement line located at the outer edge of the gorge are mostly consistent with the corresponding experimental data. There are some differences between the results based on the wind tunnel experiments and the IDDES method in the height range of  $0.2$ – $0.4H$  on the line  $L_2$ . Considering all these, the data of measuring points at  $0.2H$  height on the measuring lines were used to further compare the differences between the experimental data and the simulation results. Therefore, Fig. 11 presents the time history curves of the wind speeds at the three typical measurement points (#1, #2, and #3) in the three cases based on the wind tunnel tests and the CFD prediction methods. Table II provides the mean wind speed ( $\bar{U}_Z$ ) and the standard deviation of the wind speed ( $\sigma_U$ ) of three typical measurement points in three cases during 4–10 s based on the wind tunnel tests and the CFD prediction methods, in which the standard deviation of the wind speed is used to reflect the fluctuation of the wind speed at the measurement points. Combined with Fig. 11 and Table II, it can be noticed that the wind speed fluctuations at measurement points #1 and #3 are close to each other, and the wind speed fluctuations at measurement point #2 are significantly larger than those at the measurement points #1 and #3. In the wind tunnel tests, the standard deviation of the wind speed at the measurement point #2 is more than

2.7, 2.6, and 2.0 times of the corresponding values at the measurement points #1 or #3 in the Case I, the Case II, and the Case III, respectively. In the CFD predictions, the standard deviation of the wind speed at the measurement point #2 is more than 3.9, 2.4, and 3.1 times of the corresponding values at the measurement points #1 or #3 in the Case I, the Case II, and the Case III, respectively. These mean that the wind speed fluctuations at the downstream of the gorge center are more dramatic compared to the downstream of the outer edge of the gorge. With the increase in mountain spacing, the standard deviation of the wind speed at the measurement point (#1, #2, and #3) decreases rapidly. As shown in Table II, the differences between the results of the wind tunnel tests and the CFD prediction methods are maintained within 6%, excluding the measurement point #2 in the Case I. Due to the shading effect of the mountain, there may be a large angle of the wind speed or backflow at point #2 in Case I, resulting in the failure of the Cobra Probe to capture the full signal of the wind speed. Therefore, it can be considered that the IDDES method used in this paper is reasonable.

##### 2. Power spectral density of wind field

Figure 12 presents the power spectra density (PSD) of wind and its fitted curves for the typical measurement point (#2) on the leeward side of the gorge in the three cases based on the wind tunnel tests and the CFD prediction methods. As shown in Fig. 12, the PSD values of the typical measurement points (#2) in different cases are stably distributed in the 0–10 Hz band (shaded area in the figure) in both the wind tunnel tests and the CFD prediction methods. In the wind tunnel tests, the mean PSD value ( $1.56 \times 10^{-3}$ ) of the point #2 in the Case I within the 0–10 Hz band is 2.2 and 9.33 times higher than the corresponding values ( $7.1 \times 10^{-4}$  and  $1.672 \times 10^{-4}$ ) of the point #2 in the Case II and the Case III, respectively. In the CFD prediction methods, the mean PSD value ( $6.2 \times 10^{-3}$ ) of the point #2 in the Case I within the 0–10 Hz band is 3.95 and 12.94 times higher than the corresponding values ( $1.57 \times 10^{-3}$  and  $4.793 \times 10^{-4}$ ) of the point #2 in the Case II and the Case III, respectively. The results obtained based on both methods reflect the susceptibility of the mean PSD values downstream of the gorge to the influence of mountain spacing.

Figure 12 indicates the peak of the PSD at the measurement points, and the peak of the PSD at the points is located in the frequency band of 0–10 Hz in all cases based on the wind tunnel tests and the CFD prediction method. This indicates that the wind field energy downstream of the gorge center is mainly concentrated in the 0–10 Hz band. In the wind tunnel tests, the peak of the PSD ( $1.065 \times 10^{-2}$ ) of the point #2 in the Case I is 3.37 and 14.77 times higher than the corresponding values ( $3.16 \times 10^{-3}$  and  $7.21 \times 10^{-4}$ ) of the point #2 in the Case II and the Case III, respectively. In the CFD prediction methods, the peak of the PSD ( $3.56 \times 10^{-2}$ ) of the point #2 in the Case I is 7.64 and 15.08 times higher than the corresponding values ( $4.66 \times 10^{-3}$  and  $2.36 \times 10^{-3}$ ) of the point #2 in the Case II and the Case III, respectively. This means that the peak of the energy in the wind field downstream of the gorge center is inversely proportional to the spacing of the mountains. The peak of energy in the wind field downstream of the gorge center differs by an order of magnitude among the three cases.

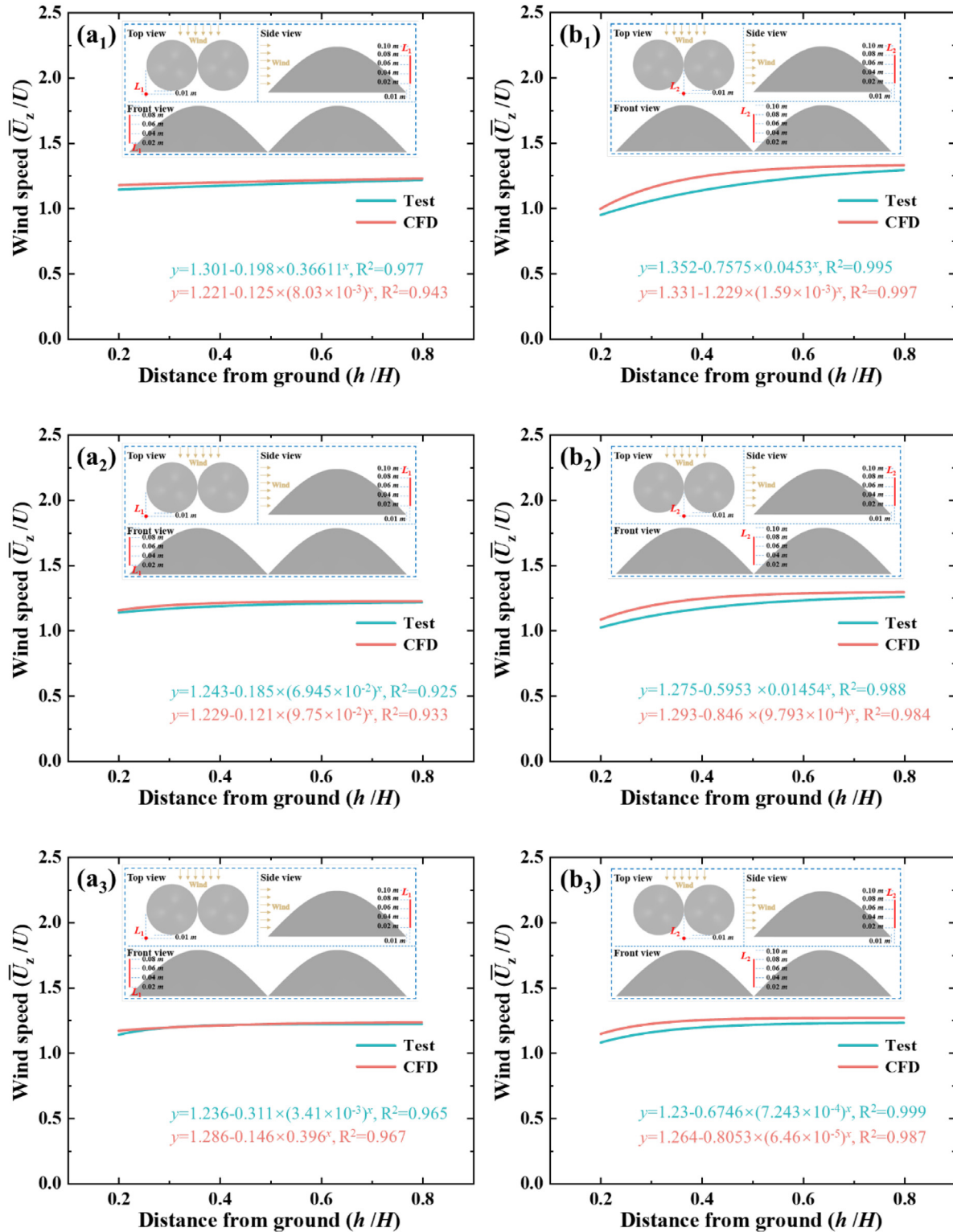


FIG. 10. The comparison of the distribution of the Z component of the mean wind speed along the lines in Y direction: (a) L<sub>1</sub>; (b) L<sub>2</sub>: (Subscripts 1, 2, and 3 indicate the Case I, the Case II, and the Case III, respectively).

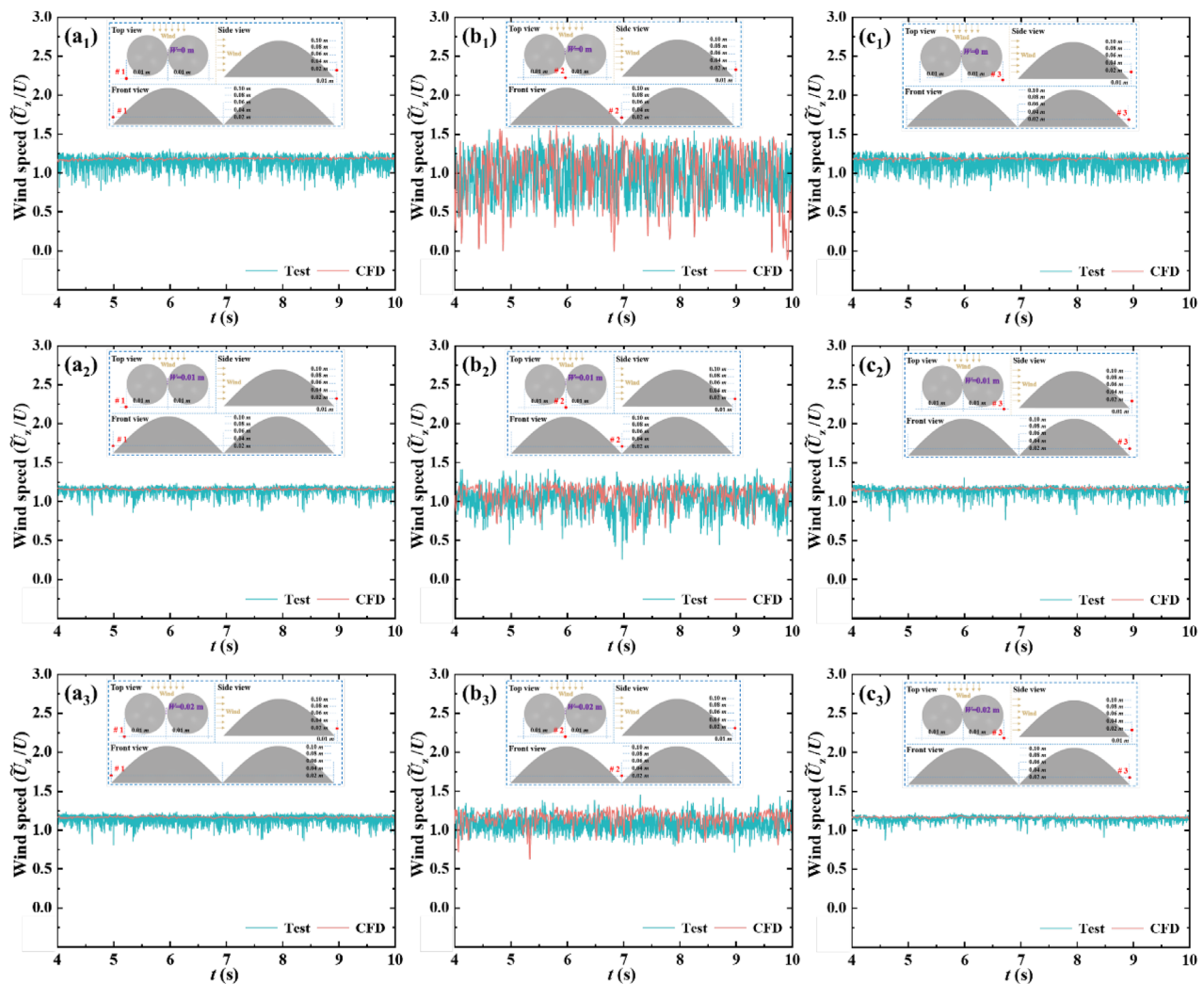


FIG. 11. The time history curve of the Z component wind speed at three typical measurement points: (a) #1; (b) #2; and (c) #3: (Subscripts 1, 2, and 3 indicate the Case I, the Case II, and the Case III, respectively).

TABLE II. The Z component of the mean wind speed ( $\bar{U}_Z$ ) and the standard deviation of the wind speed ( $\sigma_U$ ) of three typical measurement points in three cases during 4–10 s.

Case		# 1		# 2		# 3	
		$\bar{U}_Z$	$\sigma_U$	$\bar{U}_Z$	$\sigma_U$	$\bar{U}_Z$	$\sigma_U$
Case I	Test	1.138	0.088	0.946	0.241	1.144	0.083
	CFD	1.172	0.083	0.992	0.328	1.175	0.084
Case II	Test	1.133	0.050	1.021	0.142	1.138	0.054
	CFD	1.153	0.047	1.08	0.136	1.156	0.051
Case III	Test	1.136	0.031	1.076	0.092	1.137	0.028
	CFD	1.16	0.029	1.142	0.091	1.16	0.027

## B. The effect of Reynolds number on the results

The Reynolds number is a dimensionless number used to characterize the flow state presented by a flow field and also reflects the ratio of inertial to viscous forces in a fluid. The influence of viscous force on the flow field is greater than inertia when the Reynolds number is small, and the disturbance of the flow velocity in the flow field will be decayed due to the viscous force, and the flow state of the fluid is manifested as laminar flow. At larger Reynolds number, the effect of inertia on the flow field is greater than viscous force, fluid flow is more unstable, and small changes in flow velocity are easy to develop, enhance, and form a turbulent, irregular turbulent flow field. The Reynolds number is mainly influenced by the size of the model and the incoming wind speed. This section analyzes the effect of the incoming wind speed and the size of the model on the results of the wind tunnel tests and the CFD prediction.

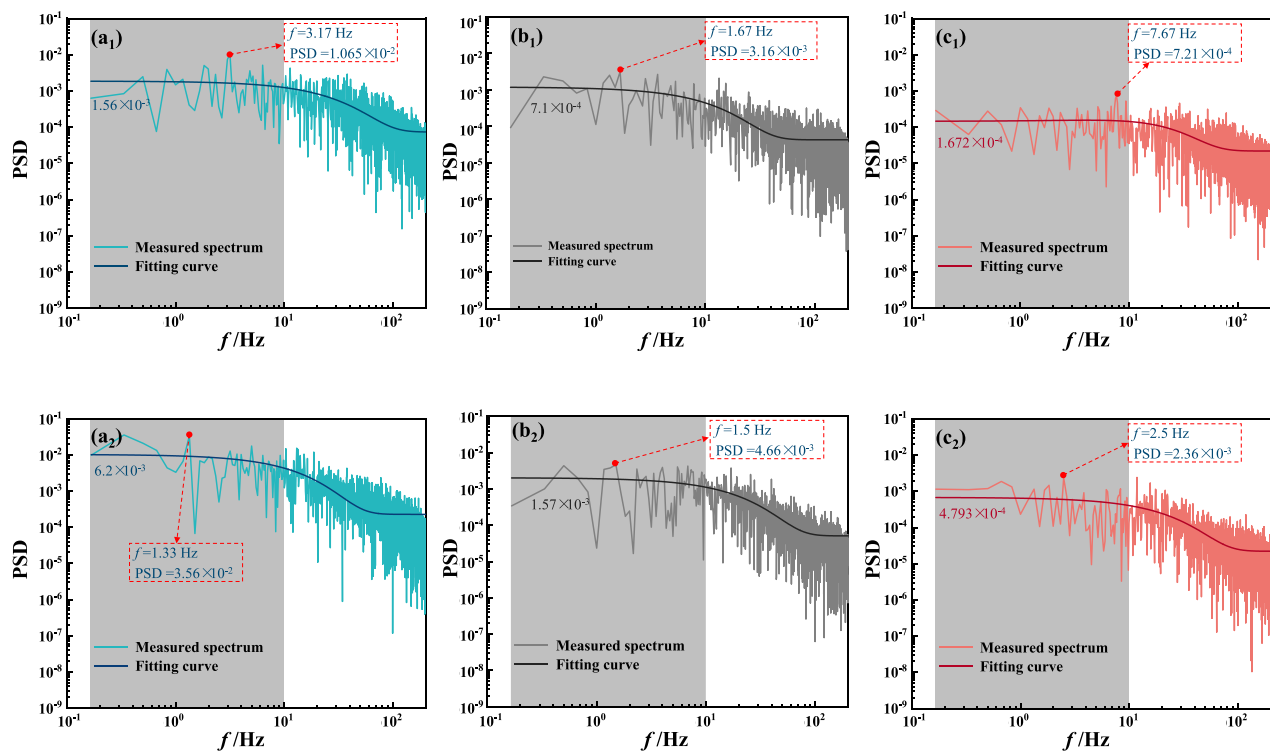


FIG. 12. The PSD at the typical measuring points (#2) on the leeward side of the gorge: (a) Case I; (b) Case II; and (c) Case III: (Subscripts 1 and 2 indicate the wind tunnel test and the CFD prediction method, respectively).

Based on the Case I with an incoming wind speed of 29.6 m/s, the wind tunnel test systems with the incoming wind speeds of 17.81 and 23.51 m/s are established to analyze the effect of the Reynolds number on the results of wind tunnel tests. The Reynolds numbers for the three kinds of cases (17.81, 23.51, and 29.6 m/s) are calculated to be  $1.22 \times 10^5$ ,  $1.61 \times 10^5$ , and  $2.03 \times 10^5$ , respectively. A case in BS

EN 14067-4 (Ref. 36) requires that the Reynolds number for wind tunnel tests should be more than  $2.5 \times 10^5$ . Figure 13(a) presents the time history curves of the Z component of the wind speed at the measured points under the effect of the three kinds of incoming flows (17.81, 23.51, and 29.6 m/s) for the experimental model with a mountain spacing of 0 m. As shown in Fig. 13(a), the fluctuations of the

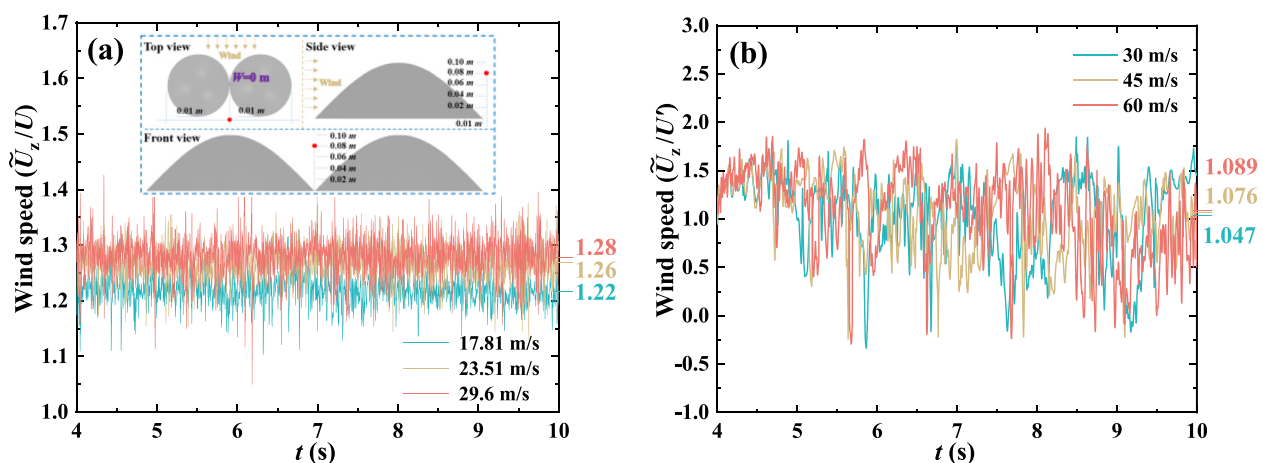


FIG. 13. The time history curves of the Z component of the wind speed at the measured points under the effect of the different incoming flows for the models with a mountain spacing of 0 m: (a) the test model with a scaling ratio of 1:500; (b) the CFD model with a scaling ratio of 1:10.

wind speed at the measurement points on the leeward side of the gorge under the effect of the three kinds of incoming flows (17.81, 23.51, and 29.6 m/s) are quite consistent. The mean values of the wind speed at the measurement points during 4–10 s are 1.22, 1.26, and 1.28, respectively. The difference between the mean wind speeds of the measured points in the cases with the incoming wind speed of 17.81 and 23.51 m/s is 3.28%, and the difference between the mean wind speeds of the measured points in the cases with the incoming wind speed of 23.51 and 29.6 m/s is 1.59%. It can be assumed that the effect of the Reynolds number on the wind field can be neglected when the wind speed of the incoming flow reaches 23.51 m/s or more.

Based on the GM-0 case with an incoming wind speed of 30 m/s, the CFD models with the incoming wind speeds of 45 and 60 m/s are established to analyze the effect of the Reynolds number on the results of the CFD simulation. The Reynolds numbers for the three kinds of cases (30, 45, and 60 m/s) are calculated to be  $1.03 \times 10^7$ ,  $1.54 \times 10^7$ , and  $2.05 \times 10^7$ , respectively. Based on the Reynolds number effect,<sup>37,38</sup> it can be assumed that the mean and instantaneous flow field structures predicted based on 30 m/s incoming wind are not significantly affected by the higher Reynolds number. Figure 13(b) presents the time history curves of the Z component of the wind speed at the measured points P3 under the effect of the three kinds of incoming flows (30, 45, and 60 m/s) for the CFD model with a mountain spacing of 0 m. As shown in Fig. 13(b), there is no significant difference in the fluctuation of the wind speed at the measurement points in the three kinds of cases (30, 45, and 60 m/s), which fluctuate between  $-0.5$  and  $2.0$  m/s. The differences between the Z component of the mean wind speeds at the P3 measurement points in the cases (45 and 60 m/s) and the corresponding value in the case of 30 m/s are 2.77% and 4.01%, respectively.

Figure 14 presents the distribution of the Z component of the mean wind speed on the line  $L_{x-1}$  in the CFD models with different scaling ratios (1:10 and 1:500). The wind speeds at the measurement points are dimensionless using the wind speed of the incoming flow (30 and 29.6 m/s), respectively. The Reynolds numbers for the two

kinds of cases (1:10 and 1:500) are calculated to be  $1.03 \times 10^7$  and  $2.03 \times 10^5$ , respectively. As shown in Fig. 14, the distribution laws of the mean wind speed on the measurement line in the CFD model with the scaling ratio of 1:10 and 1:500 are largely consistent. The highest wind speeds on the measurement line in the two cases (1:10 and 1:500) are 1.254 and 1.175, respectively, with a difference of 6.3%. Meanwhile, the difference in the maximum variation of the mean wind speed on the line is 6.4%, and the difference in the mean wind speed at the center of the line in the two cases is maintained at 5.3%. These show that the variations in the wind field characteristics are controlled to within 6.5% when the scaling ratio causes the Reynolds number to vary from  $2.03 \times 10^5$ – $1.03 \times 10^7$ .

### C. Spatial and temporal distribution of wind speed

Figure 15 presents temporal profiles of the Z component of the wind speed at five measurement points (P1, P2, P3, P4, and P5) on the leeward side for cases GM-0, GM-0.5, GM-1, and GM-7 during 4–10 s. Here,  $U'$  is the value of the wind speed set along the boundary of incoming flow and was set to 30 m/s. A time segment of 0.03 s was selected according to fluctuations in the wind speed at measurement point P3 in the time domain. It was divided into four moments ( $t_1$ ,  $t_2$ ,  $t_3$ , and  $t_4$ ) with a time spacing (0.01 s), and these components were used as the temporal nodes for the subsequent transient analysis.

As shown in Fig. 15, a significant fluctuation of the wind speed was observed at the measurement point P3 in the case GM-0. However, the wind speed at P3 for cases GM-0.5 and GM-1 fluctuated relatively gently. The fluctuations in it at P3 in case GM-0 case (1.75) were 4.3 and 4.6 times larger than those in cases GM-0.5 and GM-1 (0.41 and 0.38), respectively. This shows a significant correlation between mountain spacing and the irregularity of the wind field downstream of the gorge center in the temporal domain. Notably, the fluctuations in wind speed at measurement point P3 largely coincided with those at P1 and P5 in case GM-7 [Fig. 15(d)]. The acceleration effect existing downstream of the center of the gorge is basically consistent with the downstream of the outer edge of the gorge when the mountain spacing reaches 7 m. In addition, the wind at measurement points P2 and P4 was mainly directed along the negative Z direction owing to gyre vortices generated by the incoming flow on both sides of the mountain.

Figures 16–18 present the distribution of the Z component mean wind speed on the leeward side and at the center of the gorge during 4–10 s in four cases (GM-0, GM-0.5, GM-1, and GM-7). Considering Figs. 16 and 17 together shows that there was a significant acceleration in airflow in both the external and internal regions of the edge of the gorge. The maximum wind speed in the downstream region of the center of gorge was  $1.4U'$ . The maximum wind speeds at three heights ( $0.4H'$ ,  $0.6H'$ , and  $0.8H'$ ) downstream of the center of gorge in case GM-0 were 9.6%, 12.9%, and 12.1% higher than those in case GM-7, respectively. A comparison of the distributions of wind speed on the line of measurement in cases GM-0, GM-0.5, and GM-1 shows that sudden changes in wind speed near the center of the measurement line gradually became moderate with the increase in height. The curve of distribution of wind speed near the center of the leeward side of the mountain was sharp, but the wind speed gradually decreased at the center of the measurement line. The distribution of the wind speed on the measurement line was asymmetric, and the wind speed characteristics of the wind field on the leeward side of the gorge show significant inhomogeneity over the spatial domain. This was owing to the

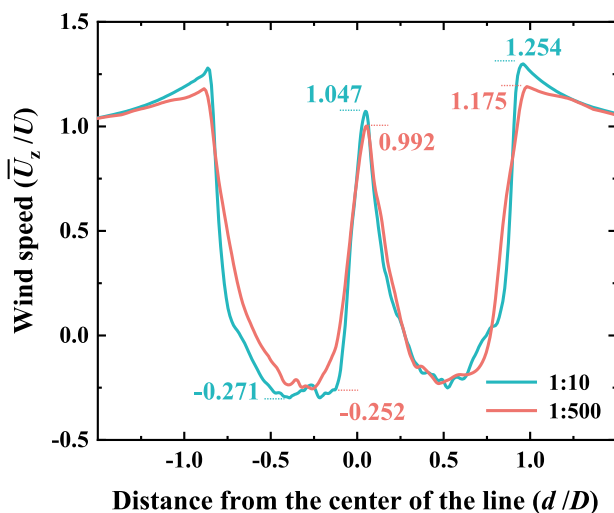


FIG. 14. The comparison of the distribution of the Z component of the mean wind speed on the line  $L_{x-1}$  in the CFD models with different scaling ratios.

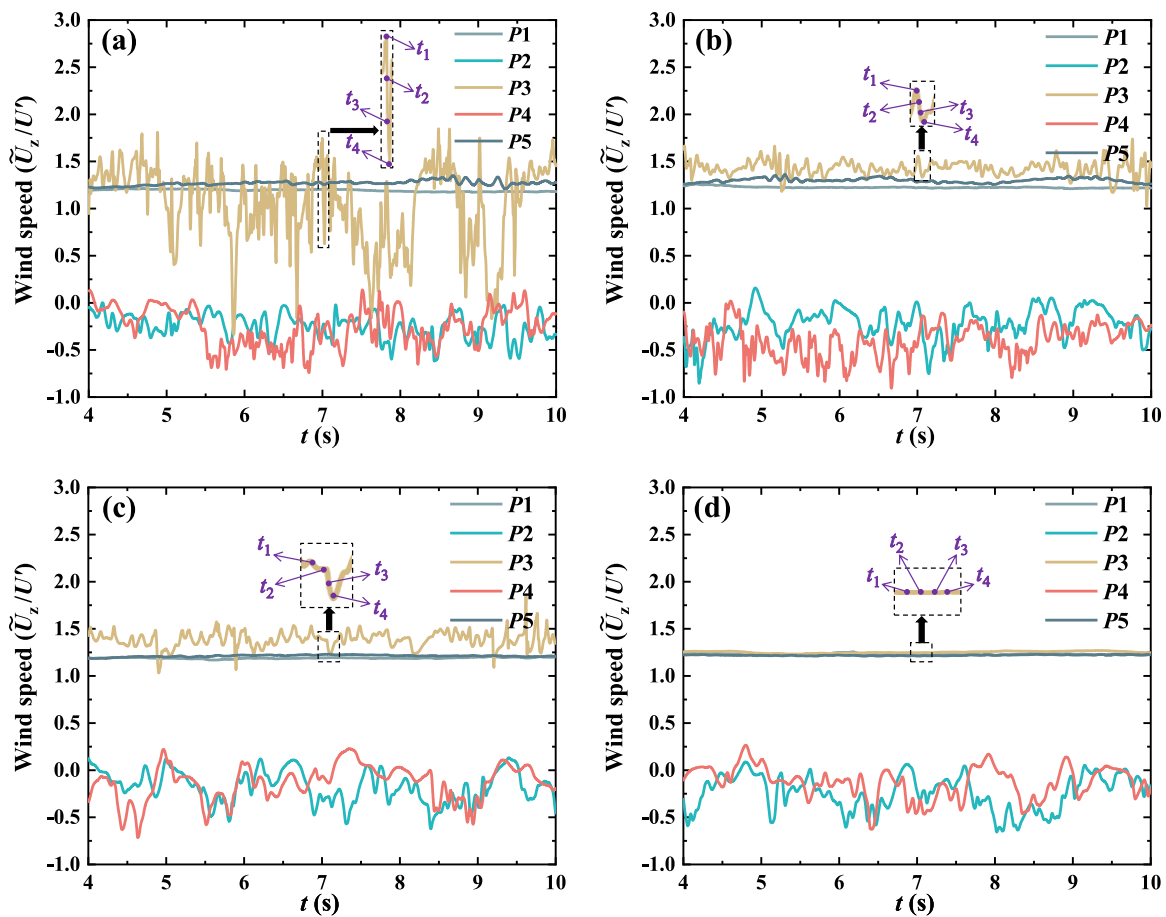


FIG. 15. The time history curve of Z component wind speed: (a) GM-0; (b) GM-0.5; (c) GM-1; and (d) GM-7.

periodic shedding of anti-symmetric double-line vortices on both sides of the mountain when the steady flow bypassed it to form a Kármán vortex street.<sup>39,40</sup> Interfering effects of vortices shedding in the center of the gorge cause wind speeds on the leeward side of the gorge to remain in an unsteady state.

Figure 16(d) shows that the peaks of wind speed on the line of measurement in cases GM-0, GM-0.5, and GM-1 decreased, which means that the points at which it peaked in the middle of the measurement line began to increase from one to two when the height was  $0.8H'$ . Based on this characteristic, the case GM-7 was used to investigate whether the same separation of the points of peak wind speed would occur at a height of  $0.2H'$ . A clear separation of the points of peak wind speed near the center of the line of measurement at  $0.2H'$  was noted in Fig. 16(a) in case GM-7. The wind speed exhibited a symmetric distribution on the measurement line, which implies that the effect of mutual interference of the two wake-induced vortices disappeared when the mountain spacing reaches 7 m. This in turn shows that there was a critical interval during which the characteristics of fluid flow suddenly changed. In the case of small spacings, the interference by the wake-induced vortex was dominant and decreased with increasing spacing between mountains. Figure 17 shows that the maximum wind speeds at four heights ( $0.2H'$ ,  $0.4H'$ ,  $0.6H'$ , and  $0.8H'$ ) in

case GM-0 were 30.1%, 23.6%, 19.7%, and 17.4% higher than the corresponding values in case GM-7, respectively. The smaller the spacing of the mountains, the smaller the area of the channel for incoming flow on the inside of the gorge, which accelerates the oncoming flow. Meanwhile, the slopes of the hills have a weaker blocking effect on the incoming flow compared to the square and cylindrical columns. These resulted in a more significant acceleration effect in the gorge with a mountain spacing of 0 m compared to a mountain spacing of 7 m.

Figure 16(a) shows that the wind speed at the center of the measurement line in case GM-0 was lower than in the other cases. A similar phenomenon was noted concerning the curves of distribution of the velocity of wind along the Z direction in Fig. 17(a), where the velocity of wind along the Z direction started to decrease early in case GM-0. Figure 18 shows that there was a significant region of low wind speed close to the ground once the incoming flow had reached the gorge, and rapidly disappeared with the increase in the mountain spacing. When the spacing of the mountains is small, the mountains provide more resistance to the incoming flow. Most of the incoming flow passes by higher locations ( $>0.2H'$ ) and outside the gorge, resulting in a lower wind speed near the ground ( $<0.2H'$ ) downstream the center of the gorge.

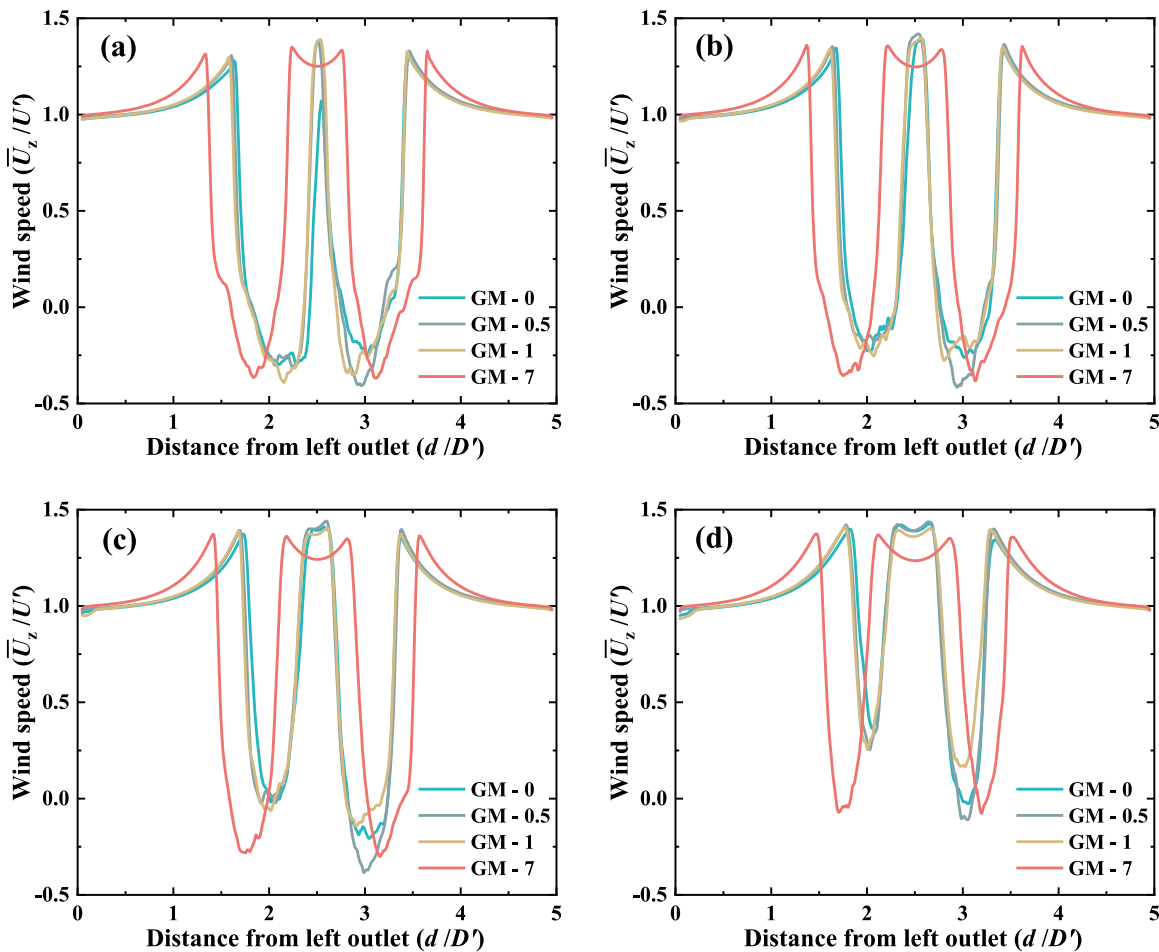


FIG. 16. The distribution of Z component mean wind speed along four lines in X direction: (a)  $L_{x1-1}$ ; (b)  $L_{x1-2}$ ; (c)  $L_{x1-3}$ ; and (d)  $L_{x1-4}$ .

#### D. Turbulence intensity

The turbulence intensity is used to describe the degree of variation of wind speed over time and space, which reflects the relative strength of pulsating wind speeds. Figure 19 presents cloud plots of the mean distributions of the intensity of turbulence in horizontal sections for cases GM-0, GM-0.5, GM-1, and GM-7 at four heights ( $0.2H'$ ,  $0.4H'$ ,  $0.6H'$ , and  $0.8H'$ ) during 4–10 s. Figure 20 shows the mean distributions of the intensity of turbulence at four measurement lines ( $L_{x1-1}$ ,  $L_{x1-2}$ ,  $L_{x1-3}$ , and  $L_{x1-4}$ ) in the X direction along the leeward side of the gorge during 4–10 s. Figure 19 shows that there were large areas of high turbulence near the shear layer on both sides of the mountain. They were caused by the frequent shedding of the uniform, steady incoming flow in this region during flow over the wall of the slope of the mountain. The area of high turbulence near measurement point P3 gradually separated with the increase in height in cases GM-0, GM-0.5, and GM-1. A comparison of the effects of the mountain spacings in Figs. 19(a<sub>1</sub>)–19(d<sub>1</sub>) shows that there was an area of high turbulence near P3 in case GM-0. With the expansion of the mountain spacing, a clear trend of separation was noted near P3 in the horizontal plane at a height of  $0.2H'$  in case GM-0.5. Finally, complete separation was obtained in case GM-7.

The analysis in Fig. 20 shows that the intensity of turbulence fluctuated sharply near the shear layer (shaded area in the figure) on both sides of the mountain. The intensity of turbulence in the leeward region of the gorge gradually increased with the height. Relative to the maximum intensity of turbulence on the measurement line in case GM-0.5, the corresponding maximum intensities of turbulence in case GM-0 increased by 15.4%, 6.4%, 5.5%, and 1.3% at the four heights ( $0.2H'$ ,  $0.4H'$ ,  $0.6H'$ , and  $0.8H'$ ), respectively. When analyzed together with Fig. 19(a<sub>1</sub>), this might have occurred owing to the mutual interference of the wake-induced vortices that frequently shed at the two mountains. As the mountain spacing increases, a distinct low-turbulence region gradually appears near the point P3. This implies that the interaction between vortices and the non-stationary characteristics of the flow between the mountains has gradually weakened.

#### E. Transient evolution of flow field

Figure 21 presents the evolution of the transient flow field for each of the four models with different mountain spacings on a horizontal profile at a height of  $0.2H'$ . The illustrations of the four moments ( $t_1$ ,  $t_2$ ,  $t_3$ , and  $t_4$ ) are provided in Fig. 15. The red dashed lines

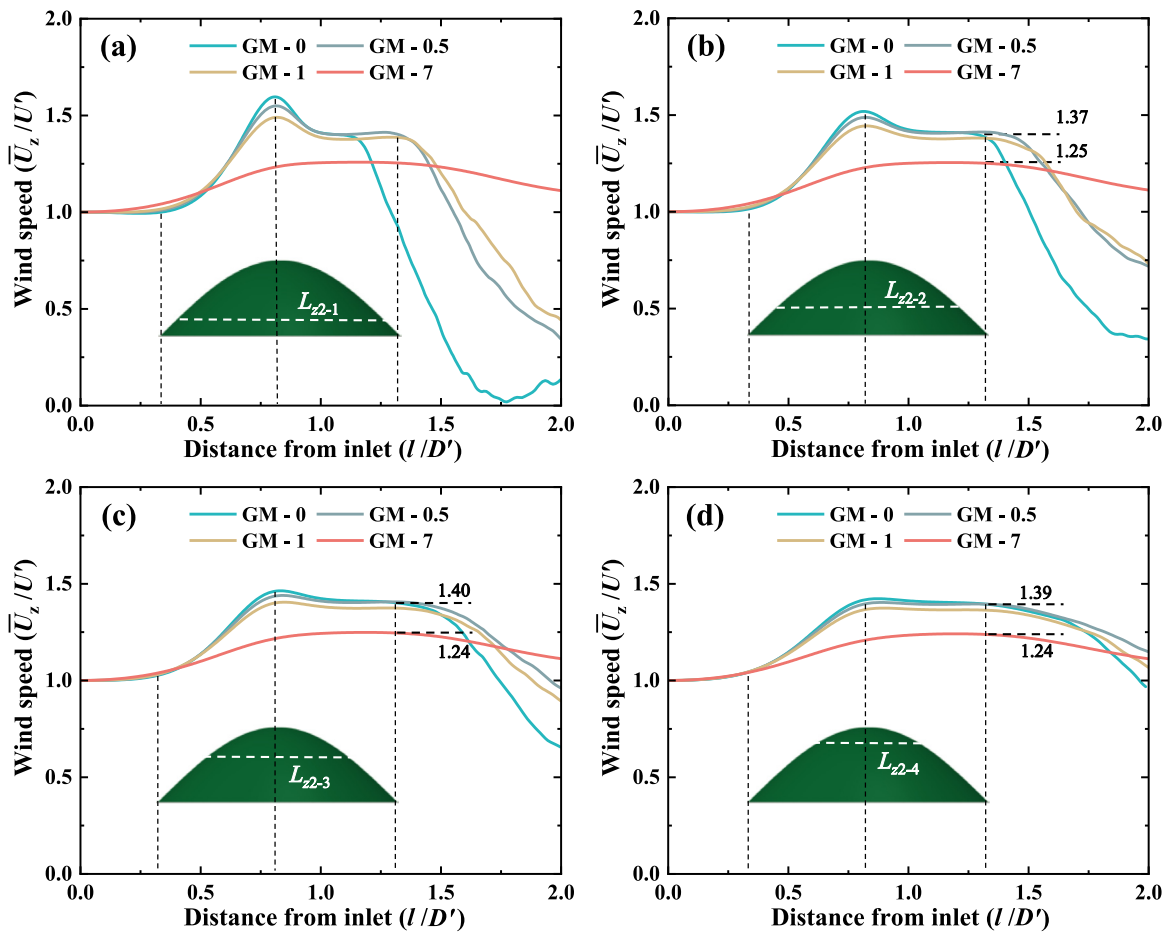


FIG. 17. The distribution of Z component mean wind speed along four lines in Z direction: (a)  $L_{z2-1}$ ; (b)  $L_{z2-2}$ ; (c)  $L_{z2-3}$ ; and (d)  $L_{z2-4}$ .

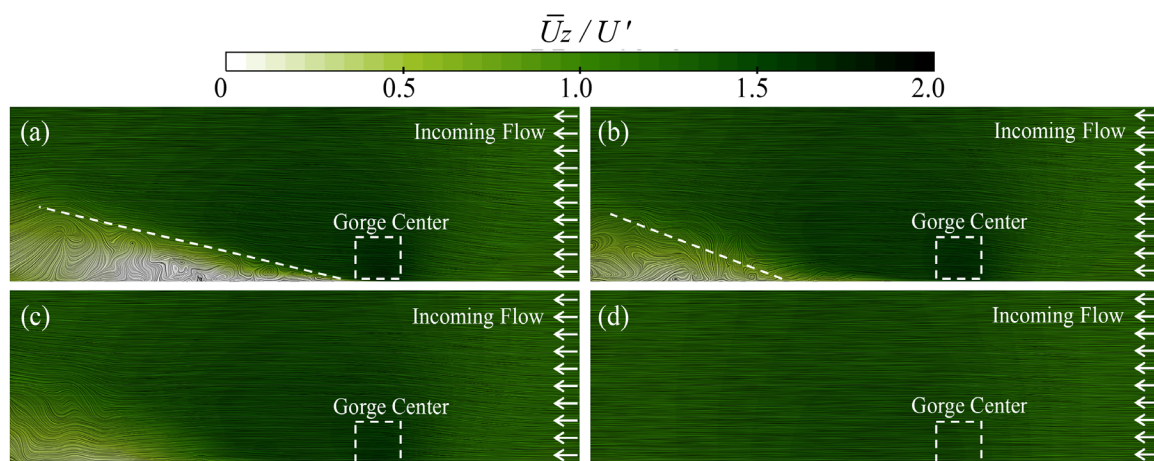
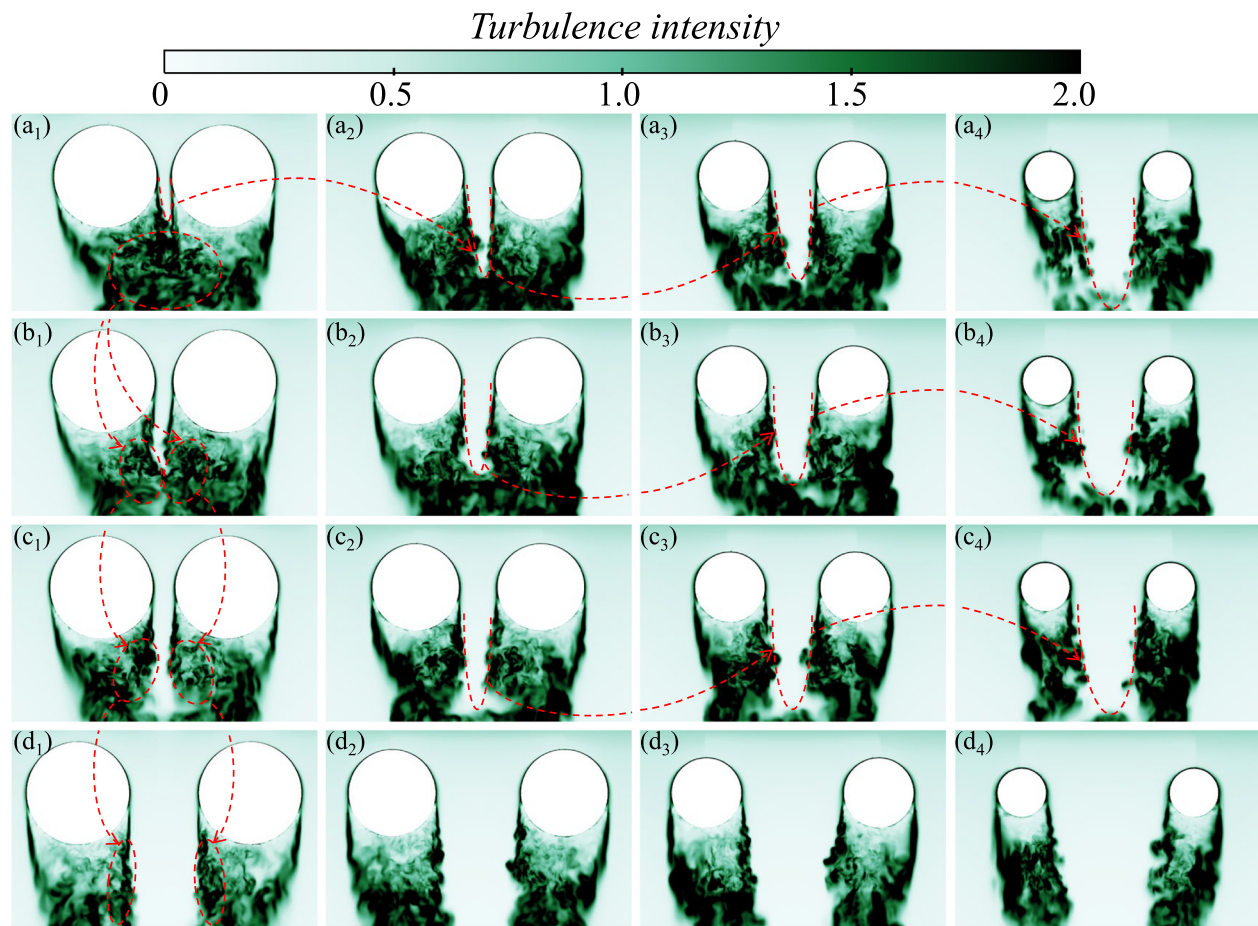


FIG. 18. The distribution of Z component mean wind speed on the longitudinal profile along the Z direction at the center of gorge: (a) GM-0; (b) GM-0.5; (c) GM-1; and (d) GM-7.



**FIG. 19.** The distribution of average turbulence intensity on the horizontal profile of the gorge: (a) GM-0; (b) GM-0.5; (c) GM-1; and (d) GM-7. (Subscripts 1, 2, 3, and 4 indicate that the horizontal profile was  $0.2H'$ ,  $0.4H'$ ,  $0.6H'$ , and  $0.8H'$  from the ground respectively).

in the figure represent the main areas of distribution of the eddy structures downstream of the center of gorge, and the blue dashed lines are used to mark the evolution process of some vortex structures. For example, the vortex structures marked in Figs. 21(a) and 21(d) gradually shrink; one large vortex structure gradually splits into two small vortex structures in Fig. 21(b). The vortex structure marked by Fig. 21(c) gradually expands during  $t_1-t_2$  and gradually shrinks during  $t_2-t_4$ . Figure 21(a) shows that the vortex that was shed downstream of the center of gorge was intense, and its distribution was irregular under mutual interference by the wake-induced vortices. The rule of evolution of this transient flow field was consistent with the non-constant nature derived from analyses of the wind speed and the intensity of turbulence. The number of vortices downstream of the center of gorge decreased in Fig. 21(b) relative to that in case GM-0 due to an increase in the mountain spacings, and the vortex moved mainly downstream. In addition, as can be seen from the enlarged images in Figs. 21(a) and 21(b), the number of vortex structures shed on the left side is higher than that on the right side in the GM-0 and GM-0.5 cases. The vortex structures downstream of the gorge oscillated to the left in cases GM-0 and GM-0.5, which indicates that the flow field of the gorge had a

biased flow regime. As shown in Figs. 21(c) and 21(d), the direction of motion of the vortex downstream of the center of gorge tilted toward the outer sides of the gorge.

#### IV. DISCUSSION

In wind tunnel testing, the test platform and instrumentation limit the placement of measurement points, and it is impossible to obtain a full set of wind field characteristics in the gorge. In addition, malfunctioning of the instrumentation results in partial invalidation of data, which is not easily detected during the experiment and reduces the efficiency of the test. These problems are more difficult to solve in field measurements than wind tunnel tests. In order to reconstruct the unknown or damaged signals from the known signals, this study attempts to use RNN algorithm to achieve it, and the RNN is the most commonly used algorithm for processing time series.<sup>41,42</sup> Figure 22 presents the structure of the RNN, and the series of four signals at 4–8 s are used for training. On the basis of the trained model, the series of signal 4 at 4–10 s is reconstructed using the series of three signals at 4–10 s. Memorization of the RNN is achieved through the connections between the nodes in the hidden layer, which is manifested in the fact

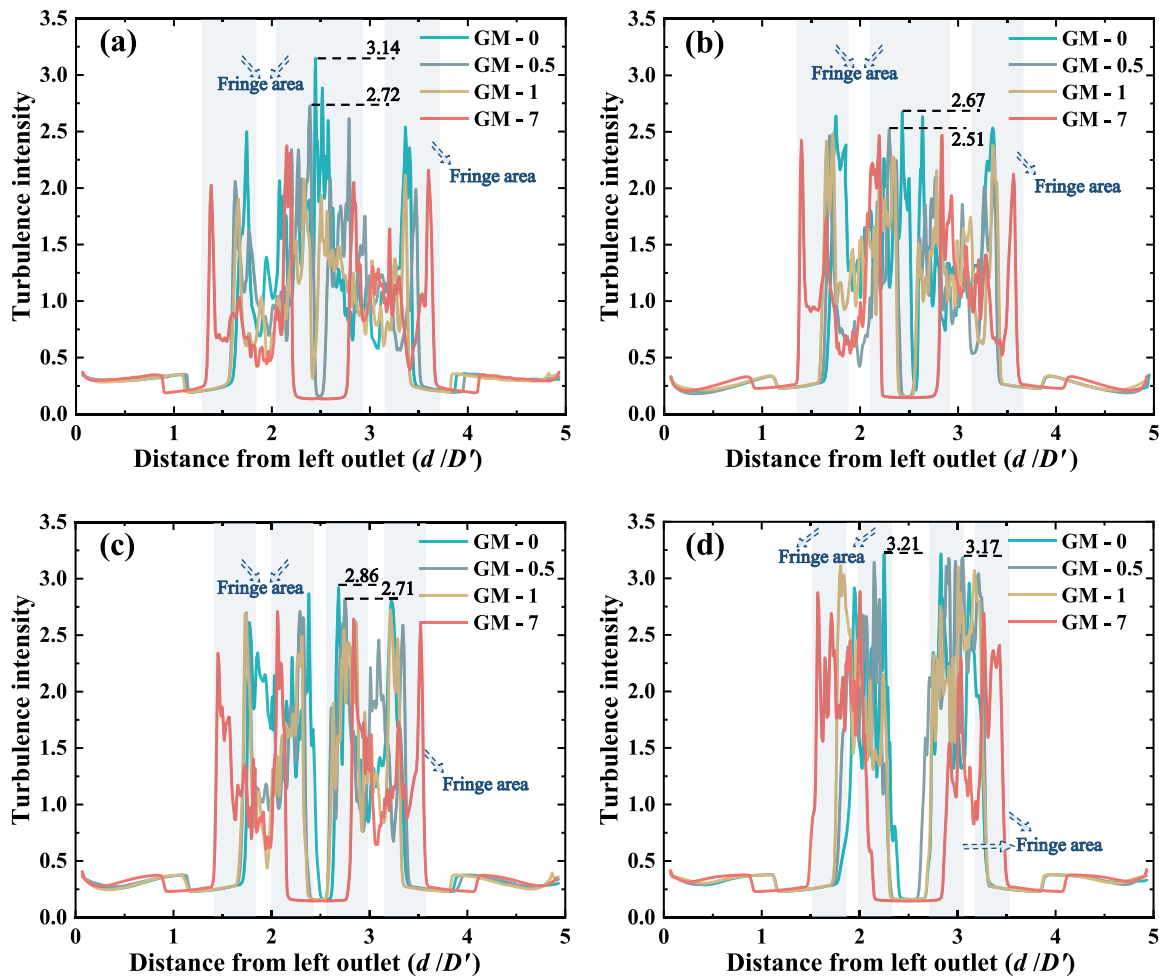


FIG. 20. The distribution of turbulence intensity along four lines in X direction: (a)  $L_{x1-1}$ ; (b)  $L_{x1-2}$ ; (c)  $L_{x1-3}$ ; and (d)  $L_{x1-4}$ .

that the network memorizes the information about the network state at the previous moment and applies it to the computation of the network state at the next moment. The network shares parameters at different locations in the hidden layer, allowing an arbitrary length sequence to be processed using a finite number of parameters. In addition, there are obvious nonlinear features in the time series of the measurement points, which indicate the feasibility of the RNN.

At the same height in the GM-0 (scaling ratio of 1:10) where the mountain spacing is 0, the Z component of the wind speeds at measurement points P3, P6 (2 m upstream of P3), P7 (2 m downstream of P3), P8 (4 m downstream of P3), P9 (6 m downstream of P3), and P10 (8 m downstream of P3) during 4–8 s are used for training (Fig. 23). Based on the trained model, the signal values of P8, P9, and P10 at 4–10 s are reconstructed using the signal values of three measurement points (P3, P6, and P7) at 4–10 s. Figure 24 compares the signal reconstruction values of P8, P9, and P10 with the corresponding calculated values obtained by CFD method during 4–10 s. The mean square error (MSE) between the reconstructed and computed values of P8 in the

training set (4–8 s) is 0.0006, and the MSE between the reconstructed and computed values of P8 in the test set is 0.0009. The MSE between the reconstructed and computed values for P9 and P10 in the training set is 0.0005 and 0.0006, respectively. The MSE between the reconstructed and calculated values for both P9 and P10 in the test set is 0.0007. Due to the memory of the trained model for the signal values of P8, P9, and P10 over a period of 4–8 s, the MSE in the training set is lower than in the test set. This means that the training model has a strong applicability to signal reconstruction at the same height. The lower connectivity of the training objects when reconstruction of signals from measuring points at different heights makes it essential to add more physical information to the model.

## V. CONCLUSION

In this study, the scaled-down (1:500) models of a gorge with three kinds of mountain spacings (0, 0.01, and 0.02 m) were established based on the wind tunnel test and the CFD prediction method. Under the effect of steady crosswind incoming flow ( $U = 29.6$  m/s),



FIG. 21. The evolution of vortex structure on the horizontal profile at a height of  $0.2H'$  in the gorge: (a)  $GM-0$ ; (b)  $GM-0.5$ ; (c)  $GM-1$ ; and (d)  $GM-7$ .

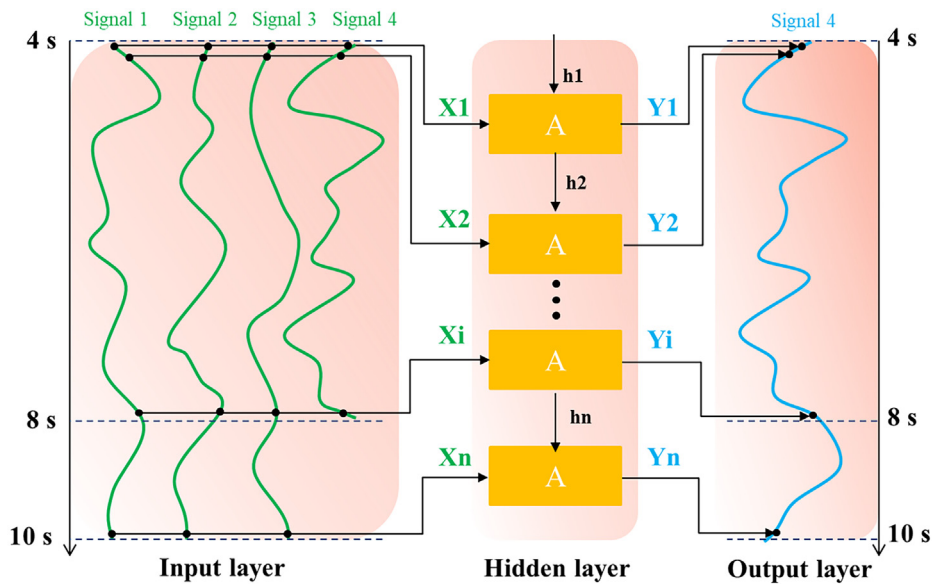


FIG. 22. Structure of the RNN.

the acceleration effect in the gorge terrain is revealed based on the wind speed and the spectrum feature of the measure points. Next, the scaled-down (1:10) models of a gorge with four kinds of mountain spacings (0, 0.5, 1, and 7 m) were established based on the IDDES method. The influence of Reynolds number on the acceleration effect is analyzed by varying the wind speed of the incoming flow and the scaling ratio of the model. Under the effect of steady crosswind incoming flow at 30 m/s, the mechanism of the effect of the mountain spacing on the acceleration is revealed based on the spatial and temporal distribution, turbulence characteristics, and evolution of the transient vortex structures. The following conclusions can be drawn:

- (1) The special topography of the gorge leads to an accelerating effect of the incoming crosswinds, the most significant acceleration reaching 1.28–1.4 times the incoming wind speed, which occurs in the gorge center.
- (2) In wind tunnel testing, the wind field energy downstream of the gorge center is mainly concentrated in the 0–10 Hz band. The peak PSD ( $1.065 \times 10^{-2}$ ) in this region of the gorge model with a mountain spacing of 0 m is 3.37 and 14.77 times higher than the corresponding values ( $3.16 \times 10^{-3}$  and  $7.21 \times 10^{-4}$ ) in the gorge topography with a mountain spacing of 0.01 and 0.02 m, respectively.

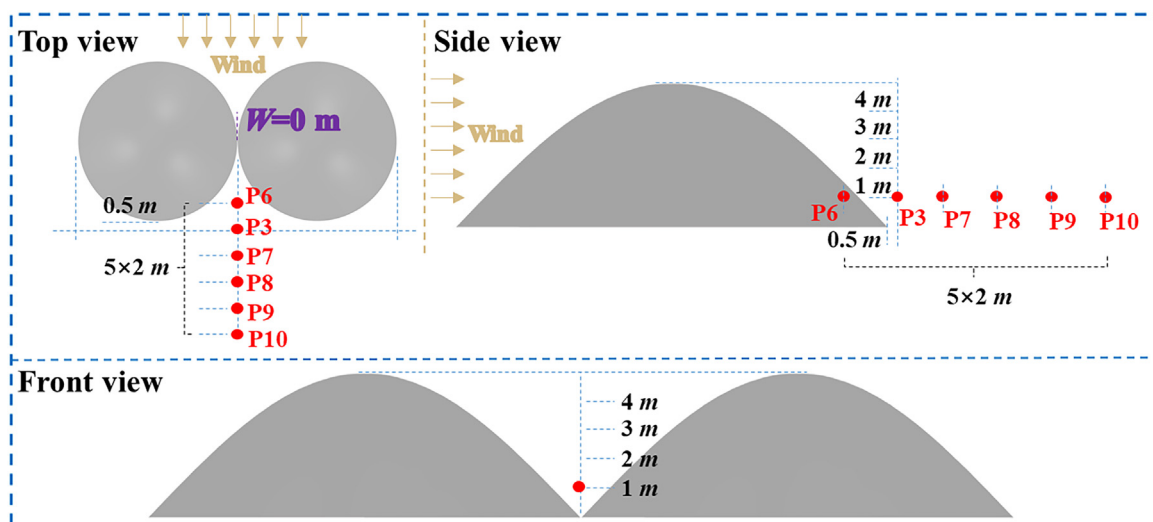


FIG. 23. Distribution of measurement points.

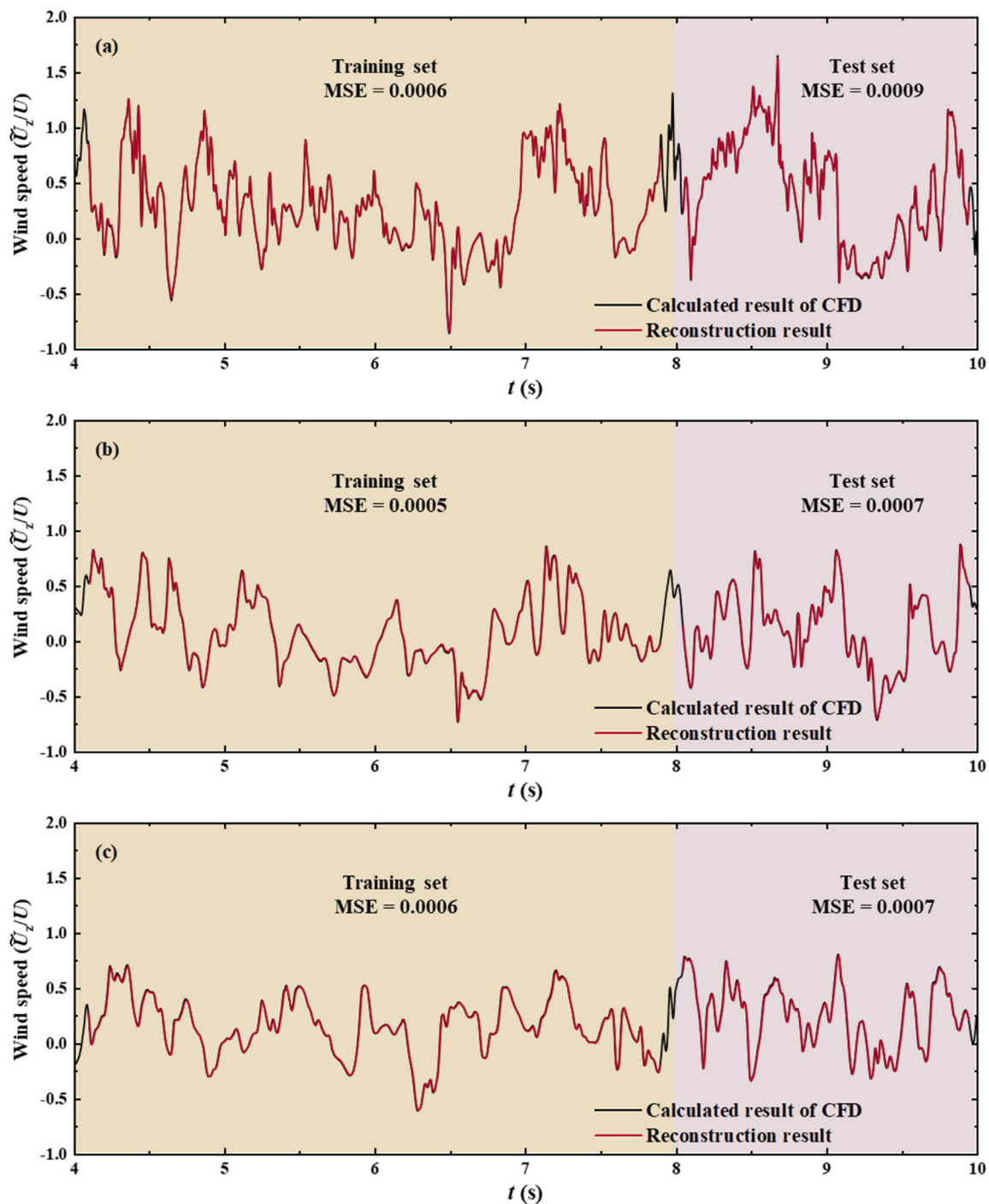


FIG. 24. Comparison of reconstructed and calculated results for the measurement point: (a) P8; (b) P9; and (c) P10.

(3) The Reynolds number has an impact on the experimental and predicted results of the gorge wind field. The maximum difference of mean wind velocities in the leeward side of the gorge is 6.4% when the Reynolds number ranges from  $2.03 \times 10^5$  to  $1.03 \times 10^7$ .

(4) When the mountain spacing is zero, the progressively narrower channel upstream of the gorge accelerates the wind velocity performance of the incoming flow. A large number of detached eddies shed on the inner edge of the gorge interfere with each

other, and the flow field downstream of the center of the gorge exhibits significant non-stationarity. Meanwhile, the acceleration effect in this zone is further increased.

The work here provides theoretical guidance for the siting and anti-wind design of transportation facilities, high-speed trains, and aircraft passing through gorges. In the future, field testing of gorge topography will be carried out. Meanwhile, the WRF-LES and RAMS prediction methods will be applied to compare the differences with CFD prediction results. In this study, signal reconstruction at the same height is attempted, and this gains success. In order to achieve signal reconstruction at different heights, it is indispensable to further supplement the physical information of the terrain in the recurrent neural network. In addition, a jet-based idea (the layout location of the air curtain machine is presented in Secs. II B 1 and II B 2) is taken to mitigate the acceleration effects existing in the gorge terrain. A preliminary numerical study found that the mitigation program resulted in a 57.1% reduction in wind speed fluctuations downstream of the gorge center. The mean velocity of wind and the mean peak intensity of turbulence were reduced by 14% and 80%, respectively, downstream of the gorge center. However, the air-jet-based strategy to reduce acceleration in the wind proposed here has not been applied in realistic gorge terrain. The realistic applications, the argumentation of mitigation effects, and the optimal design of the air-jet strategy will be considered in future research work.

## ACKNOWLEDGMENTS

This work was funded by the Research Grants Council, University Grants Committee of the Hong Kong Special Administrative Region (SAR), China (Grant No. R-5020-18); the Innovation and Technology Commission of the Hong Kong SAR Government (Grant No. K-BBY1); and The Hong Kong Polytechnic University's Postdoc Matching Fund Scheme (Grant No. 1-W21Q).

## AUTHOR DECLARATIONS

### Conflict of Interest

The authors have no conflicts to disclose.

### Author Contributions

**Jian Wang:** Investigation (lead); Software (lead); Writing – original draft (lead). **Xin-Yuan Liu:** Software (equal); Validation (equal); Writing – review & editing (equal). **E Deng:** Conceptualization (lead); Data curation (lead); Funding acquisition (equal); Methodology (lead); Supervision (lead); Writing – review & editing (lead). **Yi-Qing Ni:** Funding acquisition (lead); Resources (lead); Writing – review & editing (equal). **Pak-Wai Chan:** Writing – review & editing (equal). **Wei-Chao Yang:** Writing – review & editing (equal). **Yan-Ke Tan:** Methodology (equal).

## DATA AVAILABILITY

The data that support the findings of this study are available from the corresponding author upon reasonable request.

## REFERENCES

- Y. F. Zhang, J. Li, Z. W. Chen, and X. Y. Xu, "Running safety of metro train over a high-pier bridge subjected to fluctuating crosswind in mountain city," *Struct. Eng. Mech.* **76**(2), 207–222 (2020).
- Y. Cao, T. Tao, Y. J. Shi, S. Y. Cao, D. Zhou, and W. L. Chen, "Large-eddy simulation of separated turbulent flows over a three-dimensional hill using WRF and OpenFOAM," *J. Wind Eng. Ind. Aerodyn.* **236**, 105357 (2023).
- Y. R. Wu, X. H. Wu, J. X. Li, H. H. Xin, Q. Sun, and J. T. Wang, "Investigation of vortex-induced vibration of a cable-stayed bridge without backstays based on wind tunnel tests," *Eng. Struct.* **250**, 113436 (2022).
- C. Baker, F. Cheli, A. Orellano, N. Paradot, C. Proppe, and D. Rocchi, "Cross-wind effects on road and rail vehicles," *Veh. Syst. Dyn.* **47**(8), 983–1022 (2009).
- Z. Y. Yao, J. H. Xiao, and F. Q. Jiang, "Characteristics of daily extreme-wind gusts along the Lanxin Railway in Xinjiang, China," *Aeolian Res.* **6**, 31–40 (2012).
- D. Poggi, G. G. Katul, J. D. Albertson, and L. Ridolfi, "An experimental investigation of turbulent flows over a hilly surface," *Phys. Fluids* **19**(3), 036601 (2007).
- C. J. Yu, Y. L. Li, M. J. Zhang, Y. Zhang, and G. H. Zhai, "Wind characteristics along a bridge catwalk in a deep-cutting gorge from field measurements," *J. Wind Eng. Ind. Aerodyn.* **186**, 94–104 (2019).
- X. H. He and H. Li, "Review of aerodynamics of high-speed train-bridge system in crosswinds," *J. Cent. South Univ.* **27**(4), 1054–1073 (2020).
- S. Giappino, S. Melzi, and G. Tomasini, "High-speed freight trains for inter-modal transportation: Wind tunnel study on the aerodynamic coefficients of container wagons," *J. Wind Eng. Ind. Aerodyn.* **175**, 111–119 (2018).
- S. G. Perry and W. H. Snyder, "Laboratory simulations of the atmospheric mixed-layer in flow over complex topography," *Phys. Fluids* **29**, 020702 (2017).
- P. Hu, Y. L. Li, Y. Han, C. S. Cai, and G. J. Xu, "Wind tunnel tests on the characteristics of wind fields over a simplified gorge," *Adv. Struct. Eng.* **20**(10), 1599–1611 (2017).
- P. Mouzourides, C. Marakkos, and M. K. A. Neophytou, "Urban street canyon flows under combined wind forcing and thermal buoyancy," *Phys. Fluids* **34**(7), 076606 (2022).
- Z. Y. Zhang, P. Huang, G. Bitsuamlak, and S. Y. Cao, "Large-eddy simulation of wind-turbine wakes over two-dimensional hills," *Phys. Fluids* **34**(6), 065123 (2022).
- W. C. Yang, H. Yue, E. Deng, Y. W. Wang, X. H. He, and Y. F. Zou, "Influence of the turbulence conditions of crosswind on the aerodynamic responses of the train when running at tunnel-bridge-tunnel," *J. Wind Eng. Ind. Aerodyn.* **229**, 105138 (2022).
- H. M. Jing, H. L. Liao, C. M. Ma, Q. Y. Tao, and J. S. Jiang, "Field measurement study of wind characteristics at different measuring positions in a mountainous valley," *Exp. Therm. Fluid Sci.* **112**, 109991 (2020).
- J. L. Song, J. W. Li, and R. G. J. Flay, "Field measurements and wind tunnel investigation of wind characteristics at a bridge site in a Y-shaped valley," *J. Wind Eng. Ind. Aerodyn.* **202**, 104199 (2020).
- J. L. Song, J. W. Li, R. Z. Xu, and R. G. J. Flay, "Field measurements and CFD simulations of wind characteristics at the Yellow River bridge site in a converging-channel," *Eng. Appl. Comp. Fluid Mech.* **16**(1), 58–72 (2022).
- W. M. Ren, C. Pei, C. M. Ma, Z. G. Li, Q. Wang, and F. Chen, "Field measurement study of wind characteristics at different measuring positions along a bridge in a mountain valley," *J. Wind Eng. Ind. Aerodyn.* **216**, 104705 (2021).
- T. Zhou, Q. S. Yang, B. W. Yan, X. W. Deng, and Y. J. Yuan, "Detached eddy simulation of turbulent flow fields over steep hilly terrain," *J. Wind Eng. Ind. Aerodyn.* **221**, 104906 (2022).
- E. Deng, H. Yue, Y. Q. Ni, X. H. He, W. C. Yang, and Z. W. Chen, "Wake dynamic characteristics of windproof structures in embankment-bridge sections along a high-speed railway under natural strong crosswinds," *Phys. Fluids* **35**, 055109 (2023).
- W. C. Yang, Y. K. Liu, E. Deng, Y. W. Wang, X. H. He, and M. F. Lei, "Characteristics of wind field at tunnel-bridge area in steep valley: Field measurement and LES study," *Measurement* **202**, 111806 (2022).
- B. E. McGrath, B. Z. Cybyk, and T. M. Frey, "Environment-vehicle interaction modeling for unmanned aerial system operations in complex airflow environments," *Johns Hopkins APL Tech. Dig.* **31**(2), 115–131 (2012).
- T. H. Liu, Z. W. Chen, X. S. Zhou, and J. Zhang, "A CFD analysis of the aerodynamics of a high-speed train passing through a windbreak transition under crosswind," *Eng. Appl. Comput. Fluid Mech.* **12**(1), 137–151 (2018).

- <sup>24</sup>W. C. Yang, E. Deng, X. H. He, L. S. Luo, Z. H. Zhu, Y. W. Wang, and Z. T. Li, "Influence of wind barrier on the transient aerodynamic performance of high-speed trains under crosswinds at tunnel-bridge sections," *Eng. Appl. Comput. Fluid Mech.* **15**(1), 727–746 (2021).
- <sup>25</sup>E. Deng, W. C. Yang, X. H. He, Z. H. Zhu, H. F. Wang, Y. W. Wang, A. Wang, and L. Zhou, "Aerodynamic response of high-speed trains under crosswind in a bridge-tunnel section with or without a wind barrier," *J. Wind Eng. Ind. Aerodyn.* **210**, 104502 (2021).
- <sup>26</sup>E. Brambilla, S. Giappino, and G. Tomasini, "Wind tunnel tests on railway vehicles in the presence of windbreaks: Influence of flow and geometric parameters on aerodynamic coefficients," *J. Wind Eng. Ind. Aerodyn.* **220**, 104838 (2022).
- <sup>27</sup>Z. W. Chen, T. H. Liu, Z. J. Guo, X. S. Huo, W. H. Li, and Y. T. Xia, "Dynamic behaviors and mitigation measures of a train passing through windbreak transitions from ground to cutting," *J. Cent. South Univ.* **29**(8), 2675–2689 (2022).
- <sup>28</sup>E. Deng, W. C. Yang, M. F. Lei, Z. H. Zhu, and P. P. Zhang, "Aerodynamic loads and traffic safety of high-speed trains when passing through two windproof facilities under crosswind: A comparative study," *Eng. Struct.* **188**, 320–339 (2019).
- <sup>29</sup>P. Lou, W. Tao, C. Z. Cai, X. H. He, Y. F. Zou, and Y. Y. Ai, "Influence of wind barriers with different curvatures on crosswind aerodynamic characteristics of a train-bridge system," *Appl. Sci.* **12**(3), 1747 (2022).
- <sup>30</sup>Z. W. Chen, E. Z. Rui, T. H. Liu, Y. Q. Ni, X. S. Huo, Y. T. Xia, W. H. Li, Z. J. Guo, and L. Zhou, "Unsteady aerodynamic characteristics of a high-speed train induced by the sudden change of windbreak wall structure: A case study of the Xinjiang railway," *Appl. Sci.* **12**(14), 7217 (2022).
- <sup>31</sup>W. C. Yang, E. Deng, M. F. Lei, Z. H. Zhu, and P. P. Zhang, "Transient aerodynamic performance of high-speed trains when passing through two windproof facilities under crosswinds: A comparative study," *Eng. Struct.* **188**, 729–744 (2019).
- <sup>32</sup>Z. Q. Liu, W. Wang, Y. Z. Wang, and T. Ishihara, "Large eddy simulations of slope effects on flow fields over isolated hills and ridges," *J. Wind Eng. Ind. Aerodyn.* **201**, 104178 (2020).
- <sup>33</sup>Q. S. Yang, T. Zhou, B. W. Yan, M. Liu, P. V. Phuc, and Z. R. Shu, "LES study of topographical effects of simplified 3D hills with different slopes on ABL flows considering terrain exposure conditions," *J. Wind Eng. Ind. Aerodyn.* **210**, 104513 (2021).
- <sup>34</sup>A. Risan, J. A. Lund, C. Y. Chang, and L. Saetran, "Wind in complex Terrain—Lidar measurements for evaluation of CFD simulations," *Remote Sens.* **10**(1), 59 (2018).
- <sup>35</sup>E. Deng, H. Yue, Y. Q. Ni, Y. W. Wang, X. H. He, and Z. W. Chen, "A turbulent crosswind simulation method at high-speed railway tunnel entrance: Based on field test and geometric turbulence generator," *Phys. Fluids* **35**, 015156 (2023).
- <sup>36</sup>BS EN, "Railway applications-aerodynamics-Part 5: Requirements and test procedures for aerodynamics in tunnels," BS EN. 14067-4 (2013), pp. 21–22.
- <sup>37</sup>A. Sohankar, "Flow over a bluff body from moderate to high Reynolds numbers using large eddy simulation," *Comput. Fluids* **35**(10), 1154–1168 (2006).
- <sup>38</sup>M. F. Khaled and A. M. Aly, "Assessing aerodynamic loads on low-rise buildings considering Reynolds number and turbulence effects: A review," *Adv. Aerodyn.* **4**(1), 24 (2022).
- <sup>39</sup>X. L. Wang and S. Alben, "The dynamics of vortex streets in channels," *Phys. Fluids* **27**(7), 073603 (2015).
- <sup>40</sup>X. D. Bai, W. Zhang, and Y. Wang, "Deflected oscillatory wake-induced pattern behind two side-by-side circular cylinders," *Ocean Eng.* **197**, 106847 (2020).
- <sup>41</sup>H. G. Zhang, Z. S. Wang, and D. R. Liu, "A comprehensive review of stability analysis of continuous-time recurrent neural networks," *IEEE Trans. Neural Netw. Learn. Syst.* **25**(7), 1229–1262 (2014).
- <sup>42</sup>J. K. Duan, H. C. Zuo, Y. L. Bai, J. Z. Duan, M. H. Chang, and B. L. Chen, "Short-term wind speed forecasting using recurrent neural networks with error correction," *Energy* **217**, 119397 (2021).